

Inelastic dark matter with spin-dependent couplings to protons and large modulation fractions in DAMA

Stefano Scopel,^a Kook-Hyun Yoon^b

Department of Physics, Sogang University, Seoul, South Korea

E-mail: scopel@sogang.ac.kr, koreasds@naver.com

Abstract. We discuss a scenario where the DAMA modulation effect is explained by a Weakly Interacting Massive Particle (WIMP) which upscatters inelastically to a heavier state and predominantly couples to the spin of protons. In this scenario constraints from xenon and germanium targets are evaded dynamically, due to the suppression of the WIMP coupling to neutrons, while those from fluorine targets are evaded kinematically, because the minimal WIMP incoming speed required to trigger upscatters off fluorine exceeds the maximal WIMP velocity in the Galaxy, or is very close to it. In this scenario WIMP scatterings off sodium are usually sensitive to the large-speed tail of the WIMP velocity distribution and modulated fractions of the signal close to unity arise in a natural way. On the other hand, a halo-independent analysis with more conservative assumptions about the WIMP velocity distribution allows to extend the viable parameter space to configurations where large modulated fractions are not strictly necessary. We discuss large modulated fractions in the Maxwellian case showing that they imply a departure from the usual cosine time dependence of the expected signal in DAMA. However we explicitly show that the DAMA data is not sensitive to this distortion, both in time and frequency space, even in the extreme case of a 100 % modulated fraction. Moreover the same scenario provides an explanation of the maximum in the energy spectrum of the modulation amplitude detected by DAMA in terms of WIMPs whose minimal incoming speed matches the kinematic threshold for inelastic upscatters. For the elastic case the detection of such maximum suggests an inversion of the modulation phase below the present DAMA energy threshold, while this is not expected for inelastic scattering. This may allow to discriminate between the two scenarios in a future low-threshold analysis of the DAMA data.

Contents

1	Introduction	1
2	The kinematics of fluorophobic IDM	4
3	Compatibility factors	6
4	Analysis	10
5	Large modulation fractions: the Maxwellian case	17
6	Conclusions	21
A	Experimental inputs	24

1 Introduction

The visible disk of our Galaxy is believed to be embedded in a halo of Weakly Interacting Massive Particles (WIMPs). The DAMA experiment[1] has been measuring for more than 15 years a yearly modulation effect with a sodium iodide target consistent with that expected due to the Earth rotation around the Sun from the elastic scattering of WIMPs. However, many experimental collaborations using nuclear targets different from NaI and various background-subtraction techniques to look for WIMP-elastic scattering (LUX[2], XENON100[3], XENON10[4], KIMS[5–7], CDMS- Ge [8], CDMSlite [9], SuperCDMS[10], CDMS II[11], SIMPLE[12], COUPP[13], PICASSO[14], PICO-2L[15], PICO-60[16]) have failed to observe any anomaly so far, implying severe constraints on the most popular WIMP scenarios used to explain the DAMA excess, such as WIMP-nucleus elastic scattering with a cross section proportional to the square of the atomic mass number of the target or to the nuclear spin. In particular the latter scenario consists in a WIMP fermionic particle χ (either Dirac or Majorana) that recoils on the target nucleus T through its coupling to the spin \vec{S}_N of nucleons $\mathcal{N} = (p, n)$:

$$\mathcal{L}_{int} \propto \vec{S}_\chi \cdot \vec{S}_\mathcal{N} = c^p \vec{S}_\chi \cdot \vec{S}_p + c^n \vec{S}_\chi \cdot \vec{S}_n. \quad (1.1)$$

One of the main motivations of the above interaction Lagrangian is the fact that the most stringent bounds on the interpretation of the DAMA effect in terms of WIMP-nuclei scatterings are obtained by detectors using xenon (LUX[2], XENON100[3]) and germanium (CDMS[8–11]) whose spin is mostly originated by an unpaired neutron, while both sodium and iodine in DAMA have an unpaired proton: if the WIMP effective coupling to neutrons c^n is suppressed compared to that on protons c^p this class of bounds can be evaded [17, 18]. However this scenario is constrained by droplet detectors (SIMPLE[12], COUPP[13]) and bubble chambers (PICASSO[14], PICO-2L[15], PICO-60[16]) which all use nuclear targets with an unpaired proton (in particular, they all contain ^{19}F , while SIMPLE contains also ^{35}Cl and ^{37}Cl and COUPP and PICO-60 use also ^{127}I). As a consequence, this class of experiments rules out an explanation of the DAMA effect in terms of elastic WIMP-nucleus scatterings driven by the interaction (1.1) also for $c^n \ll c^p$ when standard assumptions are

made on the WIMP local density and velocity distribution in our Galaxy[15, 18]. This tension can be relaxed if the spin-dependent scenario is generalized to a wider class of interactions containing an explicit dependence of the cross section on the exchanged momentum [19–21].

In the present paper we wish to point out that an alternative approach is possible to reconcile DAMA to fluorine detectors in the above scenario with $c^n \ll c^p$: Inelastic Dark Matter (IDM)[22]. In this class of models a Dark Matter (DM) particle χ of mass m_{DM} interacts with atomic nuclei exclusively by up-scattering to a second heavier state χ' with mass $m'_{DM} = m_{DM} + \delta$. A peculiar feature of IDM is that there is a minimal WIMP incoming speed in the lab frame matching the kinematic threshold for inelastic upscatters and given by:

$$v_{min}^* = \sqrt{\frac{2\delta}{\mu_{\chi N}}}, \quad (1.2)$$

with $\mu_{\chi N}$ the WIMP–nucleus reduced mass. This quantity corresponds to the lower bound of the minimal velocity v_{min} (also defined in the lab frame) required to deposit a given recoil energy E_R in the detector:

$$v_{min} = \frac{1}{\sqrt{2m_N E_R}} \left| \frac{m_N E_R}{\mu_{\chi N}} + \delta \right|. \quad (1.3)$$

The value of the recoil energy:

$$E_R = E_R^* = \delta \mu_{\chi N} / m_N, \quad (1.4)$$

corresponding to $v_{min} = v_{min}^*$ usually coincides, as in the case of the interaction (1.1), to the maximum of the signal.

The starting point of our analysis is the observation that, when the WIMP mass is small enough and it is possible to assume that the DAMA signal is only due to WIMP-sodium scatterings¹, since v_{min}^* decreases with the target mass m_T , it is larger for fluorine (with mass $m_F \simeq 19.7$ GeV) compared to sodium (with mass $m_{Na} \simeq 21.4$ GeV). This difference in v_{min}^* may seem to be small, due to the mild dependence of $\mu_{\chi N}$ on m_T : however, precisely when m_{DM} is small the DAMA signal is produced by WIMPs in the large-speed tail of their velocity distribution $f(\vec{v})$ in the Galactic frame, where the signal can be highly sensitive to v_{min} . This is what happens in the standard Isothermal Sphere Model usually adopted to analyze direct detection data, i.e. a Maxwellian representing a WIMP gas in thermal equilibrium with r.m.s. velocity $v_{rms} \simeq \sqrt{3/2}v_{loc} \simeq 270$ km/sec (with $v_{loc} \simeq 220$ km/sec the galactic rotation curve at the Earth’s position[23]) and a velocity upper cut due to the escape velocity v_{esc} (all quantities defined in the Galactic reference frame).

In particular, indicating with v_{min}^{*Na} and v_{min}^{*F} the values of v_{min}^* for sodium and fluorine, the most extreme situation is achieved when the WIMP mass m_{DM} and the mass gap δ imply the hierarchy:

$$v_{min}^{*Na} < v_{cut}^{lab} < v_{min}^{*F}, \quad (1.5)$$

with v_{cut}^{lab} the result of the boost in the lab rest frame of some maximal value v_{cut} beyond which the WIMP velocity distribution in the Galactic rest frame vanishes (typically v_{cut} is identified

¹In this case the KIMS experiment, containing CsI , is not sensitive to the DAMA effect due to its energy threshold[5, 7]

with the WIMP escape velocity v_{esc}): in this case fluorine detectors turn outright blind to WIMP scatterings ² while DAMA not only remains sensitive to them, but it observes a modulation of the signal which represents a very large fraction of the time-averaged value, up to 100%. In fact in Eq.(1.5) the boosted value of the escape velocity v_{esc}^{lab} oscillates back-and-forth between the two constant quantities v_{min}^{*Na} and v_{min}^{*F} due to the annual change Δv_{Earth} of the Earth velocity in the Galactic rest frame between its maximal value in June and its minimal value in December. When the WIMP mass is sufficiently small $\Delta v_{Earth} \gtrsim v_{min}^{*F} - v_{min}^{*Na}$ and the amplitude of the oscillation is large enough to exceed the interval between v_{min}^{*F} and v_{min}^{*Na} : this means that in some time interval centered in December $v_{min}^{*Na} > v_{esc}^{lab}$ and also the signal in DAMA vanishes, implying a modulation fraction approaching 100%. In addition to that v_{min}^{*Na} belongs to the v_{min} interval explaining the DAMA signal and so the corresponding energy E_R^{*Na} belongs to the recoil energy interval where the signal is measured; as it will be explained in Section 5, in the Maxwellian case this implies that for $E_R = E_R^{*Na}$ the expected modulation amplitude has a maximum, since the latter is a decreasing function of v_{min} when v_{min} is large (and in particular when it is close to the escape velocity, as in our case); this feature might be in agreement with the energy dependence of the modulation amplitudes measured by DAMA, which indeed show a peak close to the threshold [1]. However this would not imply a change in sign of the modulation amplitude at lower energies, as predicted for elastic scattering of WIMPs of even lower masses[24], allowing for a possible discrimination of the two scenarios in future low-threshold analyses of modulation data in DAMA [25].

The qualitative outline summarized above will be confirmed by the quantitative analysis contained in the following Sections, where we will show that configurations $m_{DM} - \delta$ exist in the IDM parameter space (close to the condition (1.5), but allowing for some departure from it) where the DAMA annual modulation effect can be explained by a WIMP signal in compliance with other constraints. This will be achieved both by using a halo-independent approach where the dependence of the expected signal on the specific choice of $f(\vec{v})$ is factorized [26–31], and alternatively by fixing $f(\vec{v})$ to a Maxwellian distribution and factorizing instead the WIMP–nucleon point-like cross section.

The very large modulation fractions implied by our scenario necessarily imply a departure of the time-dependence of the signal from the usual cosine functional form [32]. For this reason we have also dedicated the last Section of our paper to a discussion of how the ensuing distortions compare to the DAMA published data both in time and in frequency space in the case of a Maxwellian distribution, showing that the corresponding effects are below the sensitivity of the experiment.

Our paper is organized as follows: in Section 2 we discuss the kinematic conditions that correspond to Eq.(1.5) and combine them with the additional requirements needed to evade the specific constraint of the COUPP detector, which contains iodine targets and has a recoil energy threshold lower than DAMA and KIMS; in Section 3 we describe the compatibility factors that we use in the subsequent Sections to find the allowed configurations in our Scenario; Section 4 contains our quantitative analysis; in Section 5 we provide a discussion on how the large modulation fractions arising in our scenario lead to a distortion of the time dependence of the signal, and how this effect can be accommodated by the DAMA data; Section 6 contains our conclusions. Information about our treatment of experimental data is provided in Appendix A.

²The COUPP and PICO-60 experiments contain also iodine and have an energy threshold significantly lower than KIMS: their case will be discussed separately in the next Section.

2 The kinematics of fluorophobic IDM

In the following we will assume a WIMP particle coupling to ordinary matter via the spin-dependent interaction Lagrangian of Eq.(1.1) with $c^p \gg c^n$. For this reason in this Section we will assume that bounds from detectors using xenon and germanium targets are automatically evaded (although we will come back to this issue in the numerical analysis of Section 4) and will not consider them any further, concentrating instead on detectors containing fluorine and iodine, which are sensitive to the c^p coupling. As already pointed out, when the condition of Eq.(1.5) is verified, droplet detectors and bubble chambers turn blind to WIMP scatterings off fluorine targets since WIMPs bound to the Galactic halo are not fast enough to trigger upscatters of χ to the heavier state χ' , while at the same time a population of WIMP particles with speeds below the maximal velocity v_{cut} still exists explaining the DAMA effect.

Let's first consider the (usual) case when a specific choice for the velocity distribution $f(\vec{v})$ is adopted (as in the case of a Maxwellian). In this case v_{cut} is equal to the escape velocity v_{esc} , which can be determined from observation [33, 34]. Using Eqs.(1.2,1.3) one gets the following conditions on the two free parameters m_{DM} and δ :

$$\delta > \frac{1}{2} \left(v_{esc}^{lab} \right)^2 \mu_{\chi F} \quad (2.1)$$

$$\delta < \sqrt{2m_{Na}E_{R,b}^{DAMA}v_{esc}^{lab}} - \frac{m_{Na}E_{R,b}^{DAMA}}{\mu_{\chi Na}}. \quad (2.2)$$

Eq. (2.1) corresponds to the second inequality in Eq. (1.5), while Eq. (2.2) corresponds to the requirement that the v_{min} interval corresponding to the DAMA signal falls below v_{esc} (this latter condition is more restrictive than the first inequality of Eq.(1.5)). In particular, in the equations above $\mu_{\chi F}$, $\mu_{\chi Na}$ are the WIMP-fluorine and WIMP-sodium reduced masses, respectively, while $E_{R,b}^{DAMA}$ corresponds to the experimental recoil energy boundary of the DAMA signal that yields the stronger constraint on δ . In this Section we will neglect the effect of energy resolution and assume that the DAMA modulated signal is concentrated in the range $2 \text{ keV} \leq E_{ee}^{DAMA} \leq 4 \text{ keV}$ for the equivalent-energy $E_{ee}^{DAMA} = qE_R^{DAMA}$ (measured in keV) and $q \simeq 0.3$ the quenching factor on sodium. This implies explicitly $E_{R,b}^{DAMA} \simeq 6.7 \text{ keV}$ in Eq.(2.2).

The two curves corresponding to Eqs.(2.1) and (2.2) are shown with the the solid (green) line and the thick (red) dashes, respectively in Fig.1(a) for $v_{esc}=550 \text{ km/sec}$. In particular, by assuming the value $v_{Sun}=232 \text{ km/sec}$ for the velocity of the Solar system with respect to the WIMP halo this corresponds to $v_{esc}^{lab}=782 \text{ km/sec}$ in the lab rest frame. In this case the corresponding region of the $m_{DM}-\delta$ plane is between the two curves for $m_{DM} \gtrsim 11 \text{ GeV}$.

For the low values of m_{DM} shown in Fig.1(a) it is straightforward to show that in order for scatters off iodine both in DAMA and in KIMS to be above the corresponding thresholds large values of $v_{min} \gtrsim 900 \text{ km/sec} > v_{esc}^{lab}$ are required. However, among bubble chamber detectors both COUPP [13] and PICO-60 [16] use trifluoriodomethane targets (CF_3I) which also contain iodine. Both experiments, which have not observed any excess in their data, have energy thresholds substantially lower than DAMA and KIMS: for COUPP $E_{th}^{COUPP}=7.8 \text{ keV}$, while for PICO-60 $E_{th}^{PICO-60}=7 \text{ keV}$, yielding some constraints to our scenario. Since only a very small fraction of the livetime of the PICO-60 was operated with a threshold lower than COUPP (about 1% of the total [16]) the ensuing combined constraint is driven by COUPP, as will be shown in our numerical analysis. The COUPP bound is evaded when:

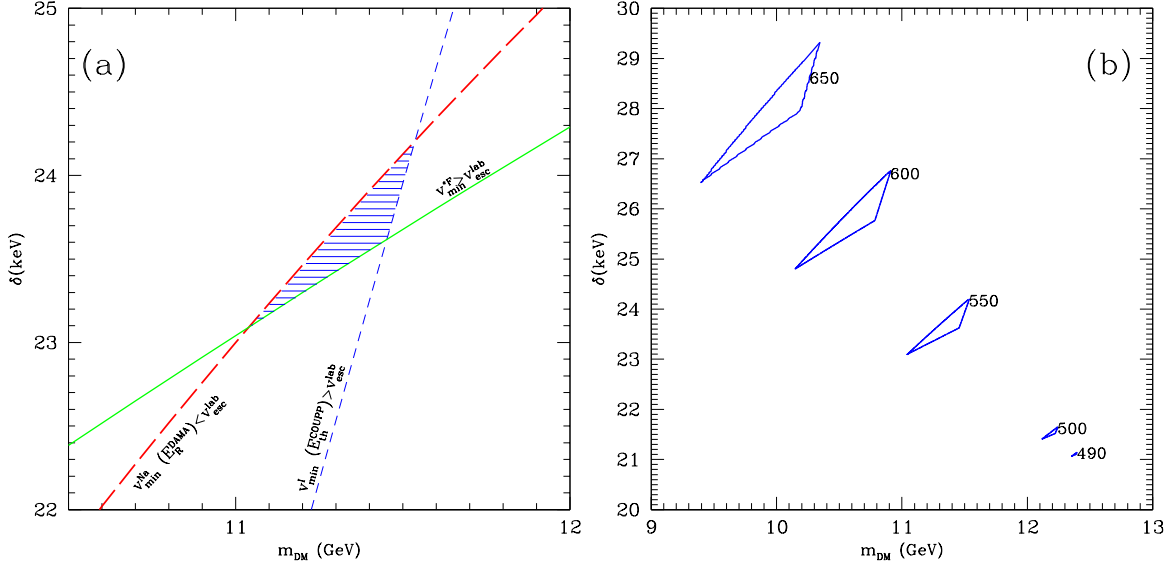


Figure 1. (a) The horizontally (blue) hatched area represents values of the IDM parameters m_{DM} and δ for which the conditions of Eqs. (2.1,2.2,2.3) are verified when $v_{esc}=550$ km/sec. (b) Different determinations of the same region are shown for the indicated values of v_{esc} .

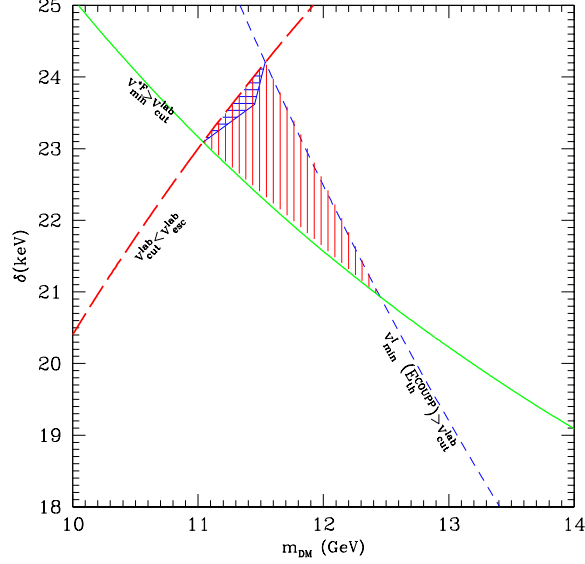


Figure 2. The vertically (red) hatched region represents the IDM parameter space where the conditions of Eqs. (2.1,2.2,2.3) are verified with $v_{esc}^{lab} \rightarrow v_{cut,DAMA}^{lab}$ equal to the highest value of v_{min} for which the DAMA effect is present (see text). The additional condition $v_{cut,DAMA}^{lab} \leq v_{esc}^{lab}$ is also enforced. The horizontally (blue) hatched area is the same shown in Fig.1(a).

$$\begin{aligned}
 & v_{min}(E^{COUPP}) > v_{esc}^{lab} \\
 \Rightarrow & \delta > \sqrt{2m_I E_{th}^{COUPP} v_{esc}^{lab}} - \frac{m_I E_{th}^{COUPP}}{\mu_{\chi I}}, \quad (2.3)
 \end{aligned}$$

with m_I the iodine nucleus mass and $\mu_{\chi I}$ the WIMP–iodine reduced mass. The corresponding curve for $v_{esc}=550$ km/sec is shown in Fig.1(a) with the (blue) dashed line.

The overlapping of the three regions corresponding to the conditions (2.1,2.2,2.3) in the $m_{DM}-\delta$ plane yields the horizontally (blue) hatched area in Fig.1(a). In Figure 1(b) we have repeated the same procedure with different values of v_{esc} , showing that such bound contours exist in a range of v_{esc} encompassing those commonly used in the literature[33, 34]³.

An alternative and more conservative approach to assess the compatibility of the DAMA result with the constraints from other experiments consists in assuming instead $v_{cut}^{lab}=v_{cut,DAMA}^{lab}$ with $v_{cut,DAMA}^{lab}$ the highest value of v_{min} for which the DAMA effect is present[21]. As discussed in Section 3, in this way the halo function defined in Eq.(3.2) is the one yielding the smaller possible count rates in other detectors in compliance with its minimal required conditions (3.5). This implies the substitution $v_{esc}^{lab} \rightarrow v_{cut,DAMA}^{lab}(m_{DM}, \delta)$ in Eqs.(2.1,2.2,2.3) with the additional constraint $v_{cut,DAMA}^{lab} \leq v_{esc}^{lab}$: the ensuing range in the IDM parameters is shown in Fig.2 by the vertically (red) hatched region. Again, here and in the following we adopt for v_{esc} the reference value $v_{esc}=550$ km/sec.

The conditions dictated by (2.1,2.2,2.3) involve only kinematics, and are not strictly necessary. Indeed, as it will be shown in the quantitative analysis of Section 4, both in the case of a Maxwellian velocity distribution and for a halo–independent approach the allowed regions in the IDM parameter space extend outside the bound regions shown in Figs.1(a) and 2 (particularly so in the latter case) when also dynamical and experimental considerations are taken into account. However, the kinematic ranges discussed in this Section can be considered as the starting seeds for a more comprehensive search of allowed IDM models in our scenario.

3 Compatibility factors

In this Section we introduce the procedures that will be used in a quantitative way in Section 4 to discuss the compatibility with other constraints of an interpretation of the DAMA effect in terms of our scenario.

The halo–independent approach [26] consists in writing the expected event rate for the WIMP–nucleus scattering process in the observed detected energy interval $E'_1 \leq E' \leq E'_2$ as [27–31]:

$$R_{[E'_1, E'_2]} = \int_0^\infty dv_{min} \tilde{\eta}(v_{min}) \mathcal{R}_{[E'_1, E'_2]}(v_{min}). \quad (3.1)$$

In the equation above the detected energy E' represents the fraction of the true nuclear recoil energy E_R which is actually measured in a given experiment (taking into account a possible quenching factor < 1 for ionization and scintillation) after convolution with the experimental energy resolution,

$$\tilde{\eta}(v_{min}) = \frac{\rho_{DM} \sigma_{ref}}{m_{DM}} \int_{v_{min}} d^3 \vec{v}_T \frac{f(\vec{v}_T)}{v_T}, \quad (3.2)$$

³However, in self–truncated Isothermal models [35] that take into account the modifications of the function $f(\vec{v})$ due to the finite size of our Galaxy the rôle of the escape velocity in the calculation of the WIMP direct detection rate is played by a maximal speed $v_{max} \lesssim 430$ km/sec well below the range of v_{esc} shown in Figure 1(b).

is the *halo-function* containing all the dependence of the expected rate on the astrophysical assumptions for the WIMP halo (ρ_{DM} represents the WIMP mass density in the neighborhood of the Sun while $f(v_T^2)$ is the WIMP velocity distribution in the target rest frame) while the response function \mathcal{R} contains the spin-dependent nuclear form factor and is specific for every detector, since it includes the effects due to the energy resolution and experimental acceptances. In the following we will adopt the form factors as calculated in [36, 37] (although at the beginning of Section 4 we will comment on different determinations in the case of xenon). For the other details regarding the response function \mathcal{R} we refer to Ref. [21]: in particular, the spin-dependent case of the interaction Lagrangian (1.1) corresponds to setting $c_k^T=0$ for $k \neq 4$ and $c_4^{0,1}=(c^p \pm c^n)/2$ in Eqs. (4.5, A1) of Ref. [21].

In Eq.(3.2) σ_{ref} represents a reference cross section, defined in the limit of vanishing transferred momentum, that we take as $\sigma_{ref} = (c^p)^2 \mu_{\chi N}^2 / \pi$ ⁴. In this way the response function \mathcal{R} will depend on the ratio $r \equiv c^n / c^p$ ⁵.

Following the same procedure, it is also possible to introduce a modulated halo function $\tilde{\eta}_1$ defined as:

$$\tilde{\eta}_1(v_{min}) \equiv [\tilde{\eta}(v_{min}, t = t_{max}) - \tilde{\eta}(v_{min}, t = t_{min})] / 2, \quad (3.3)$$

with t_{max} and t_{min} the times of the year corresponding to the maximum and to the minimum of the Earth's velocity in the Galactic rest frame. In this way, the modulated amplitudes measured by DAMA can be expressed, in analogy to Eq.(3.1), as:

$$\Delta R_{[E'_1, E'_2]} = \int_0^\infty dv_{min} \tilde{\eta}_1(v_{min}) \mathcal{R}_{[E'_1, E'_2]}(v_{min}). \quad (3.4)$$

The two halo functions $\tilde{\eta}$ and $\tilde{\eta}_1$ are subject to the very general conditions:

$$\begin{aligned} \tilde{\eta}(v_{min,2}) &\leq \tilde{\eta}(v_{min,1}) \text{ if } v_{min,2} > v_{min,1}, \\ \tilde{\eta}_1 &\leq \tilde{\eta} \quad \text{at the same } v_{min}, \\ \tilde{\eta}(v_{min} \geq v_{esc}^{lab}) &= 0. \end{aligned} \quad (3.5)$$

The first condition descends from the definition (3.2), that implies that $\tilde{\eta}(v_{min})$ is a decreasing function of v_{min} . The second is a consequence of the fact that $\tilde{\eta}_1$ is the modulated part of $\tilde{\eta}$. The last condition reflects the requirement that the WIMPs are gravitationally bound to our Galaxy. As already done in Section 2 in the following we will assume that the WIMP halo is at rest in the Galactic rest frame and we will adopt as the escape velocity of WIMPs in the lab rest frame $v_{esc}^{lab} = v_{esc}^{Galaxy} + v_{Sun}$, where $v_{esc}^{Galaxy} = 550$ km/sec and $v_{Sun} = 232$ km/sec the velocity of the Solar system with respect to the WIMP halo.

The halo-independent method exploits the fact that $R_{[E'_1, E'_2]}$ and $\Delta R_{[E'_1, E'_2]}$ depend on $f(v_T^2)$ only through the minimal speed v_{min} (given in Eq.(1.3)) that the WIMP must have to deposit at least E_R . By mapping recoil energies E_R (and so detected energies E') into same ranges of v_{min} the dependence on $\eta(v_{min})$ and so on $f(v_T^2)$ cancels out in the ratio of expected rates on different targets. In this way experimental count-rates can be exploited to get direct information on the unknown halo functions $\tilde{\eta}$ and $\tilde{\eta}_1$. In particular, given an experiment with detected count rate N_{exp} in the energy interval $E'_1 < E' < E'_2$ the combination[28]:

⁴The WIMP-proton cross section corresponds to $3/16 \sigma_{ref}$.

⁵In the following we will restrict our analysis to real values of c^n and c^p , although in the case of inelastic scattering they can be complex.

$$\langle \tilde{\eta} \rangle = \frac{\int_{v_{min}^*}^{\infty} dv_{min} \tilde{\eta}(v_{min}) \mathcal{R}_{[E'_1, E'_2]}(v_{min})}{\int_{v_{min}^*}^{\infty} dv_{min} \mathcal{R}_{[E'_1, E'_2]}(v_{min})} = \frac{N_{exp}}{\int_{v_{min}^*}^{\infty} dv_{min} \mathcal{R}_{[E'_1, E'_2]}(v_{min})}, \quad (3.6)$$

can be interpreted as an average of the function $\tilde{\eta}(v_{min})$ in an interval $v_{min,1} < v_{min} < v_{min,2}$ (an analogous argument holds for $\tilde{\eta}_1(v_{min})$, when the detected count rate represents a modulation amplitude as those measured by DAMA). The v_{min} interval is defined as the one where the response function \mathcal{R} is “sizeably” different from zero (we will conventionally take the interval $v_{min}[E_R(E_{ee,1})] < v_{min} < v_{min}[E_R(E_{ee,2})]$ with $E_{ee,1} = E'_1 - \sigma_{rms}(E'_1)$, $E_{ee,2} = E'_2 + \sigma_{rms}(E'_2)$ and $\sigma_{rms}(E')$ the energy resolution).

Following the procedure outlined above it is straightforward, for a given choice of the DM parameters, to obtain estimations $\tilde{\eta}_{1,i}^{DAMA-Na}$ of the modulated halo function $\tilde{\eta}_1(v_{min})$ averaged in appropriately chosen $v_{min,i}$ intervals mapped from the DAMA experimental annual modulation amplitudes. Using the condition $\tilde{\eta}_1(v_{min}) \leq \tilde{\eta}(v_{min})$ this allows to get lower bounds on the $\tilde{\eta}(v_{min})$ function, which can be compared to the upper bounds $\tilde{\eta}_{j,lim}$ on the same quantity derived from the data of the experiments that have reported null results⁶.

Quantitatively, for a given choice of the WIMP mass m_{DM} , of the mass difference δ and of the ratio $r = c^n/c^p$, the compatibility between DAMA and all the other results can be assessed introducing the following compatibility ratio [38]:

$$\mathcal{D}(m_{DM}, r, \delta) \equiv \max_{i \in \text{signal}} \left(\frac{\tilde{\eta}_i^{DAMA-Na} + \sigma_i}{\min_{j \leq i} \tilde{\eta}_{j,lim}} \right), \quad (3.7)$$

where σ_i represents the standard deviation on $\tilde{\eta}_i^{DAMA-Na}$ as estimated from the data, $i \in \text{signal}$ means that the maximum of the ratio in parenthesis is for $v_{min,i}$ corresponding to the DAMA excess, while, due to the fact that the function $\tilde{\eta}$ is non-decreasing in all velocity bins $v_{min,i}$, the denominator contains the most constraining bound on $\tilde{\eta}$ for $v_{min,j} \leq v_{min,i}$. The latter minimum includes all available bounds from scintillators, ionizers and calorimeters (see Appendix A of the present paper and Appendix B of Ref.[21] for a summary of the experimental inputs used in our analysis). Specifically, compatibility between DAMA and the constraints included in the calculation of Eq.(3.7) is ensured if $\mathcal{D} < 1$. Note that requiring the compatibility factor of Eq.(3.7) (with the “+” sign in the numerator) to be below unity corresponds to accepting only configurations where upper bounds do not cut into the DAMA signal region altogether. Our choice has the advantage to automatize the search of compatible regions in a simple and easily reproducible way and to be a conservative one without resorting to the more involved statistical combination of inhomogeneous data sometimes affected by large systematic uncertainties. The ensuing results should be considered as indicative and depend on the assumed C.L.

The above procedure cannot be applied to bubble chambers and droplet detectors, which are only sensitive to the energy threshold, because in this case it is not possible to map the corresponding bounds to arbitrary velocity bins. Moreover, they all contain different nuclear targets (C_2ClF_5 for SIMPLE[12], CF_3I for COUPP[13] and PICO-60[16], C_4F_{10} for PICASSO[14] and C_3F_8 for PICO-2L[15] so that it is in general not possible to factorize the $\tilde{\eta}$ function in a specific range of v_{min} . In Ref.[21] we introduced an alternative procedure to

⁶In the case of inelastic scattering the correspondence between v_{min} and E_R is no longer one-to-one, so that some value of v_{min} may correspond to two values of E_R : we avoid this by binning the energy intervals in such a way that, for each experiment, E_R^* as defined in Eq.(1.4) corresponds to one of the bin boundaries[31].

handle this class of experiments, which we summarize here: i) we use the experimental DAMA modulation–amplitudes to get a conservative piecewise estimation $\tilde{\eta}_1^{est}(v_{min})$ of the minimal $\tilde{\eta}_1$ modulated halo function compatible to the signal (see for instance the (blue) dots –short dashes in Figs.5 and 6); ii) we obtain the corresponding estimation of the unmodulated part $\tilde{\eta}^{est}(v_{min})$ by requiring that it is a decreasing function of v_{min} with $\tilde{\eta}^{est}(v_{min}) \geq \tilde{\eta}_1^{est}(v_{min})$ (an explicit example is provided by the (red) dots –long dashes in Figs.5 and 6); iii) in compliance with (3.5) and with the goal of obtaining a conservative bound, we require that the function $\tilde{\eta}$ is the *minimal* one able to explain the DAMA effect, so we assume (as discussed in the second part of Section 2) that $\tilde{\eta}^{est}(v_{min} > v_{cut,DAMA}^{lab})=0$, with $v_{cut,DAMA}^{lab}$ the highest value of v_{min} for which the DAMA effect is present; iv) we then use $\tilde{\eta}^{est}(v_{min})$ to directly calculate for each experiment among k =SIMPLE, COUPP, PICO-60, PICASSO and PICO-2L and for each energy threshold $E_{th,i}$ the expected number of WIMP events $N_{k,i}^{expected}$ and compare it to the corresponding 90% C.L. upper bound $N_{k,i}^{bound}$ (see Appendix B of Ref[21] and Appendix A of the present paper for further details).

As pointed out in the Introduction, in our scenario it is quite natural that E_R^{*Na} falls in the energy interval where the DAMA modulation amplitude has been detected. This implies the existence of pairs of energy bins in DAMA that are mapped into the same range for v_{min} : in this case one gets two different determinations $\tilde{\eta}_{1,1}$ and $\tilde{\eta}_{1,2}$ of the modulated halo function in that particular range of v_{min} which must be mutually compatible; in order to ensure this we apply the following *shape test*[39]:

$$\Delta_{ST} \equiv \frac{|\tilde{\eta}_{1,1} - \tilde{\eta}_{1,2}|}{\sqrt{\sigma_1^2 + \sigma_2^2}} \leq 1.96, \quad (3.8)$$

at the 95 % C.L.

Although in the halo-independent analysis the halo function is directly fixed to the observed values of the modulation amplitudes, there exist two cases when the ensuing total signal is not guaranteed to correspond to what observed by DAMA. The first case is when part of the DAMA region falls beyond v_{cut}^{lab} ; the second case corresponds to the situation when two DAMA energy bins are mapped into the same velocity range and we calculate the corresponding value of the halo function as the combination of the two determinations. In both cases, to ensure that a particular choice of the IDM parameters provides an acceptable explanation of the DAMA effect we require that the total modulated rate $\Delta R_{2,4}$ in the energy interval $2 \text{ keV} \leq E' \leq 4 \text{ keV}$ obtained using such halo-function determinations exceeds the 95% C.L. lower bound $\Delta R_{2,4,min}^{DAMA}=0.028$ events/kg/day on the corresponding observed quantity[1].

Then, a straightforward generalization of the compatibility factor of Eq.(3.7) is:

$$\mathcal{D}(m_{DM}, r, \delta) \rightarrow \max \left(\mathcal{D}(m_{DM}, r, \delta), \frac{N_{k,i}^{expected}}{N_{k,i}^{bound}}, \frac{\Delta_{ST}}{1.96}, \frac{\Delta R_{2,4}}{\Delta R_{2,4,min}^{DAMA}} \right). \quad (3.9)$$

In Section 4 we will also test the compatibility of the DAMA modulation effect when the WIMP velocity distribution is fixed to a standard Maxwellian. This is the usual approach adopted in the literature, where in the expression of the expected rate knowledge of $f(\vec{v})$ allows to directly factorize the cross section σ_{ref} . In this case for a fixed value of the WIMP mass (and for a choice of the local WIMP density ρ_{DM}) the whole experimental spectrum allows to get a single upper bound, or in case of an excess, a single estimation of σ_{ref} . As far as the DAMA modulation effect is concerned, we will estimate an interval

$\sigma_{DAMA}^{min} \leq \sigma_{eff} \leq \sigma_{DAMA}^{max}$ for the cross section by minimizing a χ -square of the $\tilde{\eta}_1$ function through the corresponding experimental estimations (in this case σ_{eff} is just a normalization factor of $\tilde{\eta}_1$). In the case of null experiments we will use the same energy bins used for the halo-independent approach, and add one last bin containing the whole experimental range analyzed in the experiment. For each experiment k and each energy bin i we will then calculate the corresponding upper bound σ_{ki}^{bound} .

Also in the Maxwellian analysis we apply a quality check on the corresponding prediction for the modulation amplitudes. In particular, when σ_{ref} is fixed to its best-fit value we require that the p -value of the minimal χ -square exceeds $p_{min}=0.05$.

Then, in the following Section we will adopt for the Maxwellian case the compatibility factor:

$$\mathcal{D}_{Maxwellian}(m_{DM}, r, \delta) \equiv \max \left[\max_{k,i} \left(\frac{\sigma_{DAMA}^{min}}{\sigma_{ki}^{bound}} \right), \frac{p_{min}}{p} \right]. \quad (3.10)$$

4 Analysis

In this Section we wish to discuss the compatibility with other constraints of an interpretation of the DAMA effect in terms of the IDM scenario introduced in Section 1, with couplings to nuclei driven by Eq.(1.1) and $c^n \ll c^p$. In order to do that, we will explore the IDM parameter space ($m_{DM}, \delta, r \equiv c^n/c^p$) calculating both the compatibility factor \mathcal{D} defined in Eq.(3.9) (with no assumptions on the halo function $\tilde{\eta}$ besides the minimal ones listed in Eq(3.5)), and $\mathcal{D}_{Maxwellian}$ as defined in Eq.(3.10), where, instead, a Maxwellian distribution is assumed for $f(\vec{v})$.

As already discussed in our Introduction and in Section 2, the parameter $r = c^n/c^p$ must be chosen small enough to evade the bounds from xenon detectors. To illustrate this point we provide in Fig.3 a plot of \mathcal{D} and $\mathcal{D}_{Maxwellian}$ as a function of the ratio c^n/c^p . In this Figure, for the specific choice $m_{DM}=11.4$ GeV, $\delta=23.7$ keV (chosen to be inside the horizontally (blue) hatched area of Fig1(a) and identified with the benchmark P_1 in Fig. 4) the solid lines represent \mathcal{D} and $\mathcal{D}_{Maxwellian}$ where the spin-dependent nuclear form factor for xenon is evaluated using Ref [36, 37] (i.e. the same that we use also for all the other nuclei) while (red) dots and (blue) dashes represent the same quantities where we have used only for xenon two alternative determinations of the spin-dependent form factor, Bonn-A and Nijmegen, respectively, both taken from Ref.[40]. In each case the steeper curve is for $\mathcal{D}_{Maxwellian}$ while the shallower one represents \mathcal{D} , and in order to have compatibility between DAMA and all other constraints both compatibility factors must be below 1. The fact that in Fig.3 all curves change when only the form factor of xenon is modified shows that, indeed, when the IDM parameters are chosen as explained in Section 2 the only remaining bounds are from xenon targets (actually the compatibility factor turns out to be driven by LUX which has a lower energy threshold than XENON100). Moreover, the same Figure shows that in the Maxwellian case the amount of the required cancellation between the WIMP-proton and the WIMP-neutron amplitudes in xenon is always larger than the hierarchy between the spin fractions carried by protons and neutrons (i.e. $\mathcal{D}_{Maxwellian} > 1$ for $c^n=0$ for all three determination of the form factor). This means that for the Maxwellian case the ratio c^n/c^p must be tuned to a small but non-vanishing value, which actually depends on which nuclear

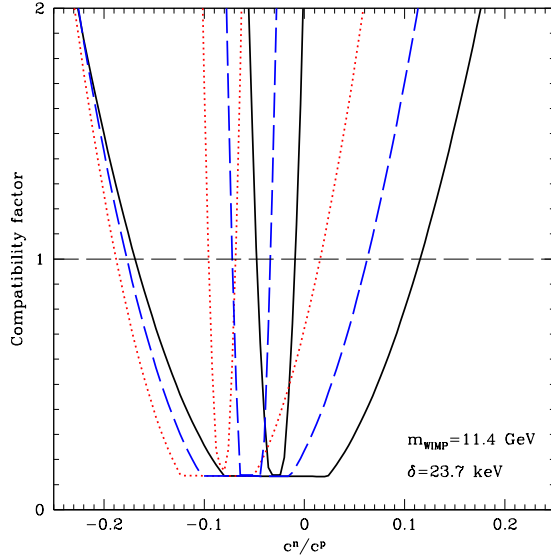


Figure 3. The compatibility factors defined in Eqs.(3.9) and (3.10) are plotted as a function of the ratio c^n/c^p for $m_{DM}=11.4$ GeV, $\delta=23.7$ keV (benchmark point P_1 in Fig.4). Solid lines: \mathcal{D} and $\mathcal{D}_{Maxwellian}$ where the xenon spin-dependent nuclear form factor is evaluated using Ref [36, 37]; (red) dots: the same curves for the Bonn-A xenon spin-dependent form factor[40]; (blue) dashes: Nijmegen xenon spin-dependent form factor[40]. In all cases the shallower curve represents \mathcal{D} while the steeper one shows $\mathcal{D}_{Maxwellian}$.

form factor is adopted. In the following analysis we will use for all nuclei the determination in [36, 37] and fix $c^n/c^p=-0.03$ which suppresses the corresponding xenon response⁷.

The result of a systematic scanning of the two compatibility factors \mathcal{D} and $\mathcal{D}_{Maxwellian}$ in the $m_{DM}-\delta$ parameter space is shown in Fig.4. In particular, the region enclosed in the (black) solid curve represents the IDM parameter space where $\mathcal{D}_{Maxwellian} < 1$, while the parameter space inside the wider (red) dotted contour has $\mathcal{D} < 1$. The regions which for kinematic reasons are not accessible to fluorine and iodine targets (discussed in detail in Section 2) are shown with (blue) horizontal hatches (Maxwellian case) and with (red) vertical hatches (halo-independent). They are the same as those shown in Figs. 1(a) and Fig. 2 and, as anticipated, cover a volume of parameter space substantially smaller than the ones with $\mathcal{D}_{Maxwellian} < 1$ and $\mathcal{D} < 1$. This figure also shows that, as expected, in the halo-independent approach, corresponding to the minimal set of assumptions for the WIMP velocity distribution, the allowed parameter space is much wider compared to the Maxwellian case.

As far as the halo-independent analysis is concerned, by numerical inspection we have determined that the lower part of the (red) dotted boundary is due to the PICASSO constraint (driven by scatterings off fluorine), while, when $m_{DM} \gtrsim 20$ GeV, the upper part of the boundary is due to COUPP (dominated by iodine). On the other hand, when 13 GeV $\lesssim m_{DM} \lesssim 20$ GeV the upper part of the dotted boundary is determined by the shape test on the DAMA modulated amplitudes, i.e. the condition $\Delta_{ST} > 1.96$ becomes more con-

⁷The corresponding values for the Bonn-A and Nijmegen form factors are $c^n/c^p \simeq -0.08$ and $c^n/c^p \simeq -0.05$, respectively, as can be seen in Fig.3.

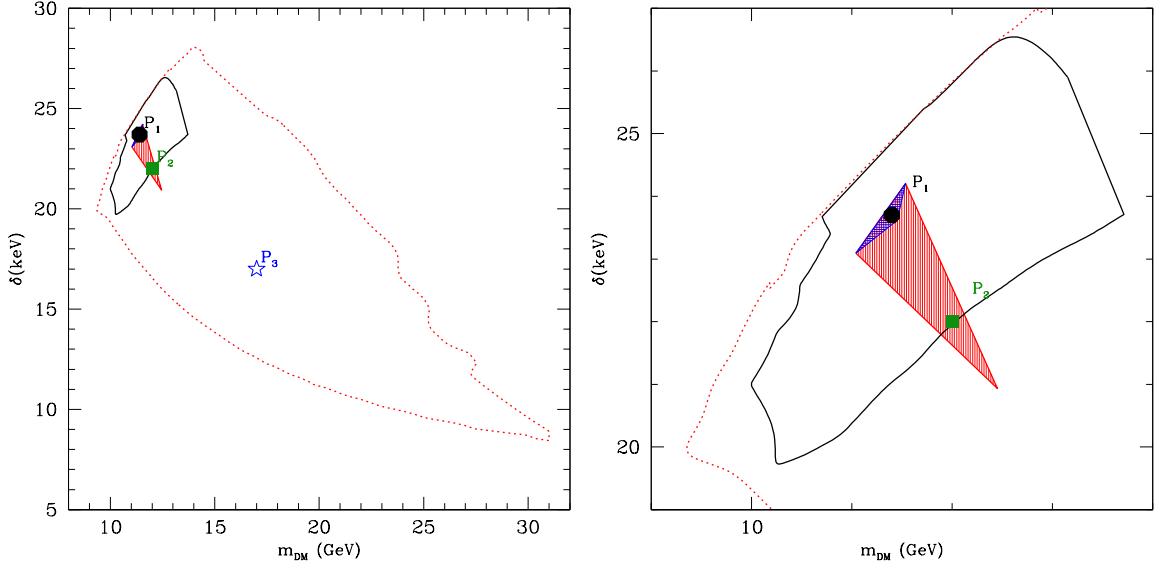


Figure 4. Contour plots of the compatibility factors \mathcal{D} (3.9) and $\mathcal{D}_{Maxwellian}$ (3.10) in the plane $m_{DM}-\delta$ for $c^n/c^p=-0.03$ (the right-handed panel is a zoom-up of the left-handed one). The region bounded by the (red) dotted contour represents configurations where $\mathcal{D} < 1$, while inside the (black) solid contour $\mathcal{D}_{Maxwellian} < 1$. The horizontally (blue) hatched area is the same shown in Fig.1(a), while the vertically (red) hatched region is the same shown in Fig.2. For the benchmark points P_1 ((black) filled circle), P_2 ((green) square) and P_3 ((blue) star) the measurements and bounds for the functions $\tilde{\eta}$, $\tilde{\eta}_1$ used to calculate \mathcal{D} and $\mathcal{D}_{Maxwellian}$ are explicitly plotted in Figs.5, 6(a) and 6(b), respectively.

straining than COUPP. Finally, in the upper part of the contour with $m_{DM} \lesssim 13$ GeV the v_{min} range explaining the DAMA effect is driven beyond v_{esc}^{lab} , so $\Delta R_{2,4} < \Delta R_{2,4}^{DAMA}$. All these behaviours (with the exception of the boundary driven by Δ_{ST}) can be qualitatively understood in terms of the kinematic boundaries discussed in Fig.2.

In Fig.4 we have also selected three benchmark points, indicated with a (black) filled circle $P_1=(m_{DM}=11.4$ GeV, $\delta=23.7$ keV), a filled (green) square $P_2=(m_{DM}=12$ GeV, $\delta=22$ keV) and a (blue) star $P_3=(m_{DM}=17$ GeV, $\delta=17$ keV), for which a detailed discussion is provided in Figs.5, 6(a) and 6(b), respectively. The benchmark P_1 lies inside the kinematic (blue) horizontally hatched area where conditions (2.1,2.2,2.3) apply. On the other hand, P_2 is outside such area but inside the (red) vertically-hatched region where in Eqs.(2.1,2.2,2.3) the conservative substitution $v_{esc}^{lab} \rightarrow v_{cut}^{lab}=v_{cut,DAMA}^{lab}$ is made. Moreover, P_2 is at the border of the $\mathcal{D}_{Maxwellian} < 1$ region. Finally, P_3 is representative of a situation where $\mathcal{D}_{Maxwellian} \gg 1$ but the more conservative halo-independent condition $\mathcal{D} < 1$ is satisfied.

In particular, in Figures 5 and 6 the measurements and bounds of the functions $\tilde{\eta}$, $\tilde{\eta}_1$ defined in Eqs.(3.2) and (3.3) and used to calculate the compatibility factors \mathcal{D} (3.7) and $\mathcal{D}_{Maxwellian}$ (3.10) for P_1 , P_2 and P_3 are shown. In such figures the (green) triangles represent the $\tilde{\eta}_1$ estimations from DAMA, where we used the modulation amplitudes of Fig.6 of Ref.[1], also reported in our Fig. 10 (the corresponding horizontal bars represent the v_{min} intervals mapped from the experimental ones on E' while the vertical bars correspond to 1σ fluctuations). On the other hand, in Figs. 5(a) and 6 the other horizontal bars show upper limits from calorimeters, ionizators and scintillators that directly measure the nuclear

recoil energy, and whose upper bounds can be mapped into v_{min} intervals (we include in our analysis LUX[2], XENON100[3], XENON10[4], CDMS-Ge[8], CDMSlite [9], SuperCDMS[10] and CDMS II[11]). Moreover, in the same figures we show with (blue) dots – short dashes a piecewise estimation of the minimal function $\tilde{\eta}_1^{est}(v_{min})$ passing through the DAMA points and with (red) dots – long dashes the ensuing minimal piecewise estimation of the function $\tilde{\eta}^{est}(v_{min})$ obtained from $\tilde{\eta}_1^{est}(v_{min})$ in compliance to the requirements of Eq.(3.5). As explained in Section 3 we use $\tilde{\eta}^{est}(v_{min})$ to calculate the expected count rates $N_{k,i}^{expected}$ used in Eq.(3.9) to obtain the compatibility factor \mathcal{D} for experiments such as droplet detectors and bubble chambers that only measure rates above a threshold and that contain different target nuclei (implying that the function $\tilde{\eta}(v_{min})$ cannot in general be directly factorized and mapped into the same v_{min} ranges of the DAMA points): in Figs. 5 and 6 the long-dashed lines show the maximal $\tilde{\eta}^{est}(v_{min})$ allowed by this class of experiments when the corresponding constraints are applied (in our analysis we include SIMPLE[12], COUPP[13], PICASSO[14], PICO-2L[15] and PICO-60[16]).

In Figure 5(b) we provide a zoom-up of Figure 5(a) where the details of how the piecewise functions $\tilde{\eta}_1^{est}(v_{min})$ and $\tilde{\eta}^{est}(v_{min})$ are obtained. In this case the energy $E_{ee}^{*Na} = qE_R^{*Na} \simeq 2.5$ keVee falls in the range 2 keVee–4 keVee where the DAMA modulation amplitudes are detected and we rebin the DAMA data so that E_{ee}^{*Na} is one of the energy boundaries and different energy bins map into same v_{min} intervals. The result of this procedure is explicitly shown in terms of the recoil energy in Fig.10, which is calculated for the same benchmark point P_1 . In particular, in Fig.10 the first and third energy bins map into the first v_{min} interval of Fig.5(b): in this case we perform the shape test of Eq.(3.8) on the ensuing two determinations $\tilde{\eta}_{1,1}$ and $\tilde{\eta}_{1,2}$ of the modulated halo function and if $\Delta_{ST} < 1.96$ the $\tilde{\eta}_1^{est}(v_{min})$ function is taken as the lower range of the statistical combination of $\tilde{\eta}_{1,1}$ and $\tilde{\eta}_{1,2}$ assuming Gaussian fluctuations.

Keeping in mind the discussion of Section 2 it is possible to understand why for the two benchmark points P_1 and P_2 an interpretation of the DAMA modulation effect in terms of WIMP inelastic scatterings is not constrained by any other experiment. In the case of P_1 , which lies in the (blue) horizontally hatched contour of Fig.4, WIMPs cannot upscatter off fluorine because the required velocity is larger than v_{esc}^{lab} , and also scatterings off iodine in COUPP are not kinematically accessible for the same reason. On the other hand, in the case of P_2 , which lies inside the (red) vertically hatched contour of Fig.4, the required WIMP incoming velocity for the same processes exceeds $v_{cut,DAMA}^{lab}$. This implies that for both P_1 and P_2 the only experiments sensitive to WIMPs besides DAMA and, to a much lesser extent, xenon and germanium detectors, are SIMPLE (due to the presence of chlorine) and PICO-2L (which contains iodine and has a threshold lower than COUPP). The maximal $\tilde{\eta}^{est}(v_{min})$ functions allowed by SIMPLE and PICO-2L, shown in Figs.5(a) and 6(a) with the lower (black) and upper (purple) long-dashed lines, respectively are well above the one which explains the DAMA effect (shown with the (red) dots – long dashes)⁸. On the other hand, the benchmark point P_3 is kinematically accessible to both fluorine and iodine in COUPP: the corresponding maximal $\tilde{\eta}^{est}(v_{min})$ function allowed by COUPP exceeds the one required to explain DAMA and is shown in Figure 6(b) with the lowest (crimson) long-dashed curve. In this case, as in all the outer region bounded by the (red) dotted contour in Fig.4, simple

⁸The small response function of chlorine (for which we use the estimation of Appendix C in Ref. [21]) and the very limited exposure collected by PICO-60[16] below the threshold of COUPP imply that the sensitivities of these two experiments are never sufficient to directly probe the DAMA effect in our scenario. For this reason we have neglected them in the kinematic discussion of Section 2.

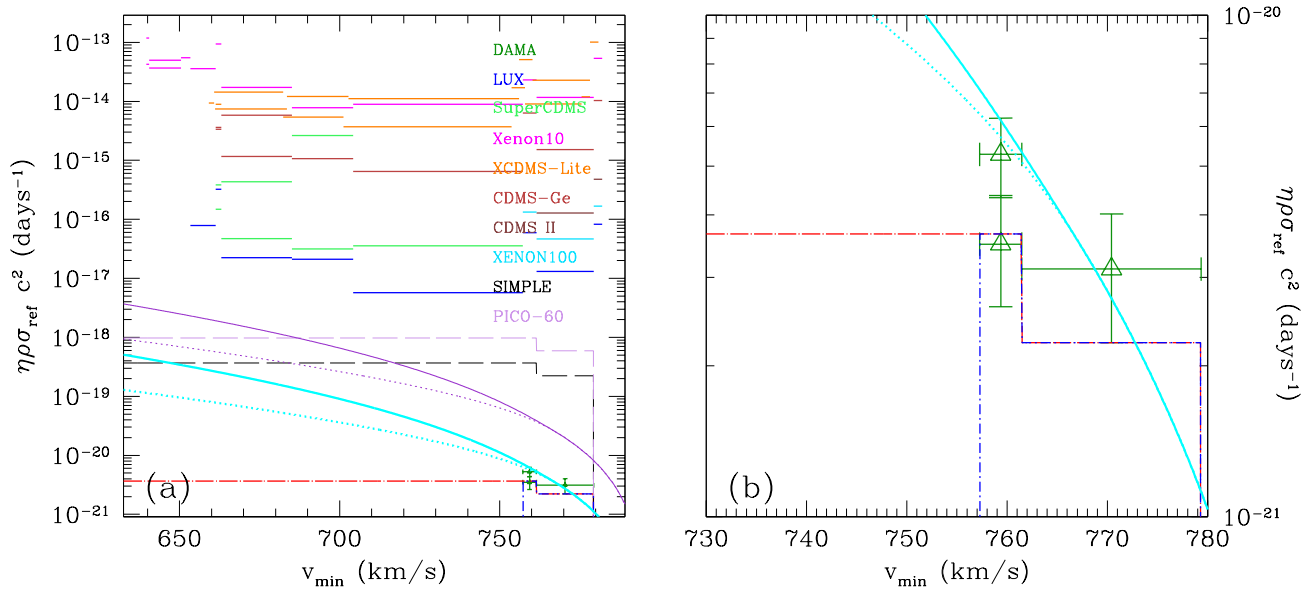


Figure 5. (a) Measurements and bounds for the functions $\tilde{\eta}$, $\tilde{\eta}_1$ defined in Eqs.(3.2) and (3.3) for $c^n/f^p=-0.03$ and $m_{DM}=11.4$ GeV, $\delta=23.7$ keV (the benchmark point P_1 indicated with a (black) filled circle in Fig.4) used to calculate the compatibility factor \mathcal{D} (3.7) and $\mathcal{D}_{Maxwellian}$ (3.10). The (green) triangles represent the $\tilde{\eta}_1$ estimations from DAMA, while horizontal lines show upper bounds from other experiments, as indicated in the plot. The thick (cyan) dotted line represents the best-fit on DAMA points of the function $\tilde{\eta}_1$ in the case of a Maxwellian distribution with $v_{esc}=550$ km/sec and $v_{rms}=270$ km/sec, while the thick (cyan) solid line is the corresponding $\tilde{\eta}$. On the other hand the (purple) thin solid line represents the maximal $\tilde{\eta}$ for the Maxwellian case allowed by PICO-2L, while the (purple) thin dotted line is the corresponding $\tilde{\eta}_1$. The (blue) dots – short dashes represent a conservative piecewise estimation of the function $\tilde{\eta}_1^{est}(v_{min})$ passing through DAMA points: (red) dots – long dashes show the corresponding minimal piecewise estimation of the function $\tilde{\eta}^{est}(v_{min})$ (in compliance to the requirements of Eq.(3.5)) used to calculate the quantities $N_{k,i}^{expected}$ of Eq.(3.9) for droplet detectors and bubble chambers (see Section 3). The lower long-dashed (black) line shows the maximal $\tilde{\eta}^{est}(v_{min})$ allowed by scatterings off chlorine in SIMPLE, while the upper (purple) one is the same curve for scatterings off fluorine in PICO-60. (b) A zoom-up of plot (a) with the details of the piecewise functions $\tilde{\eta}_1^{est}(v_{min})$ and $\tilde{\eta}^{est}(v_{min})$.

kinematic arguments cannot guarantee that a configuration is allowed: also dynamical aspects (such as the cross-section scaling laws among sodium, fluorine and iodine) and experimental issues (such as the collected data exposures and cut acceptances) are needed to ascertain the compatibility of DAMA with other experimental limits, and a full calculation of the compatibility factor \mathcal{D} (3.9) is required.

As far as the Maxwellian analysis is concerned, the lower part of the solid (black) boundary in Fig. 4 is determined by fluorine targets, namely PICO-2L for $D_M \gtrsim 11$ GeV and PICO-2L+PICASSO for $D_M \lesssim 11$ GeV. On the other hand, the right-hand side of the contour is driven by WIMP-iodine scatterings in COUPP. Finally, in the remaining left and upper parts of the contour our scenario cannot give a satisfactory interpretation of the DAMA effect because the p -value of the minimal χ -square of the DAMA modulation amplitudes corresponding to the best estimation $(\rho_{DM}\sigma_{ref})_{best}$ of $\rho_{DM}\sigma_{ref}$ is below 0.05.

In Figures 5 and 6 $(\rho_{DM}\sigma_{ref})_{best}$ is used to calculate the functions $\tilde{\eta}^{est}(v_{min})$ and

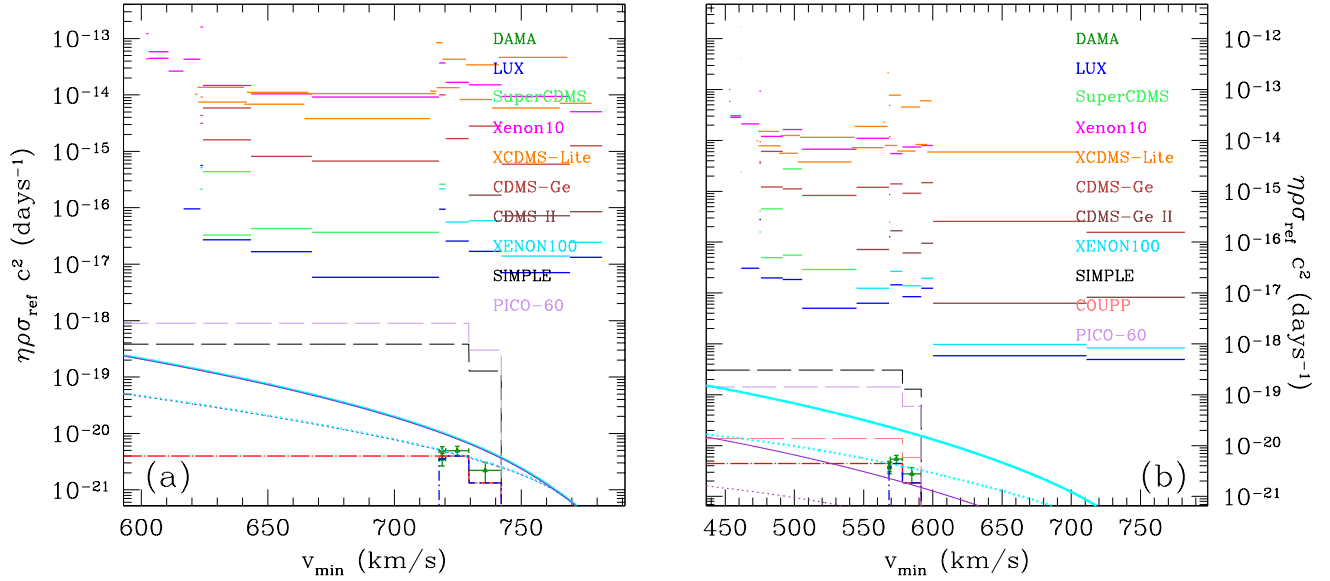


Figure 6. (a) The same as in Figure 5 with $m_{DM}=12$ GeV and $\delta=22$ keV (the benchmark point shown as a (green) square in Fig.4); (b) The same as in Figure 5 with $m_{DM}=17$ GeV and $\delta=17$ keV (the benchmark point shown as a (blue) star in Fig.4).

$\tilde{\eta}_1^{est}(v_{min})$ in the Maxwellian case: the corresponding curves are shown with the thick (cyan) solid and dotted curves, respectively. On the other hand, in the same Figures the thin (purple) solid and dotted curves represent the maximal $\tilde{\eta}_1^{est}(v_{min})$ and $\tilde{\eta}_1^{est}(v_{min})$ allowed by the most constraining among the other experiments, i.e. the two functions are calculated using the smallest among the cross section upper limits σ_{ki}^{bound} used in the compatibility factor $\mathcal{D}_{Maxwellian}$ of Eq.(3.10) for each experiment k and each energy bin i .

Also for the Maxwellian case the considerations of Section 2 can be helpful in interpreting the numerical results of Figs 5 and 6. In particular, it is clear from our previous considerations that the benchmark point P_1 is not accessible to fluorine detectors and to iodine in COUPP: indeed, in Figure 5 the σ_{ki}^{bound} used to calculate the maximal $\tilde{\eta}_1^{est}(v_{min})$ and $\tilde{\eta}_1^{est}(v_{min})$ functions is from chlorine in SIMPLE and is well above the corresponding function required to explain the DAMA effect. On the other hand, the benchmark point P_2 was chosen close to the (black) solid contour of Fig. 4 where $\mathcal{D}_{Maxwellian} \simeq 1$: for this reason in Fig.6(a) the $\tilde{\eta}_1^{est}(v_{min})$ function calculated using $(\rho_{DM}\sigma_{ref})_{best}$ is very close to the maximal Maxwellian halo function allowed by other experiments. Finally, the benchmark point P_3 is well outside the $\mathcal{D}_{Maxwellian} < 1$ parameter space, so in Figure 6(b) the best-fit estimation of the Maxwellian halo function is much above the maximal $\tilde{\eta}_1^{est}(v_{min})$ allowed by other constraints. For both P_2 and P_3 the most constraining σ_{ki}^{bound} is from PICO-2L.

The identification of $f(\vec{v})$ with a Maxwellian distribution allows the factorization of the reference cross section σ_{ref} as a function of the WIMP mass m_{DM} (at fixed δ for inelastic scattering). Indeed, this is the standard procedure adopted by experimental collaborations to present their data. For $\rho_{DM}=0.3$ GeV/cm³ we show the result of such analysis when $\delta=0$ (elastic scattering case) in Fig.7(a) while in Fig.7(b) we adopt $\delta=23$ keV. In both figures the light and dark (green) shaded areas represent the 99 % C.L. and the 95 % C.L. m_{DM} - σ_{ref} parameter space compatible to the DAMA modulation effect while open curves show

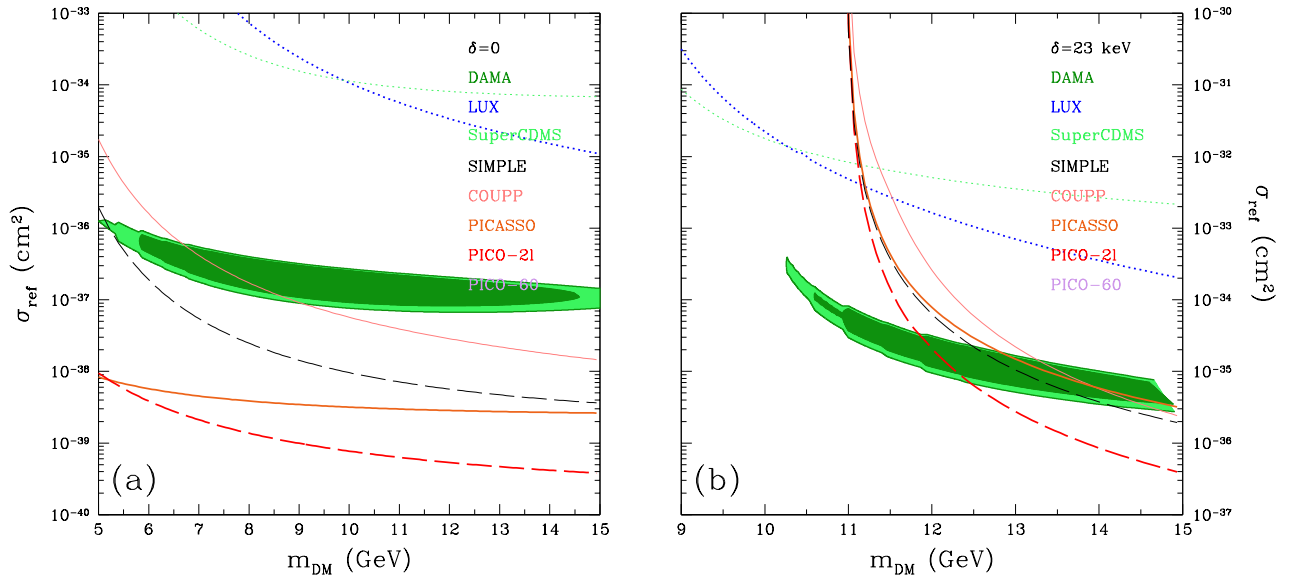


Figure 7. (a) Light and dark (green) shaded areas represent the 99 % C.L. and 95 % C.L. parameter space ranges compatible to the DAMA modulation effect in the $m_{DM}-\sigma_{ref}$ plane for $\delta=0$. Open curves show the corresponding 90% C.L. upper bounds from other experiments: LUX[2] (thick (blue) dots), SuperCDMS[10] (thin (green) dots), SIMPLE[12] (thin (black) dashes), COUPP[13] (thin (red) solid line), PICASSO[14] (thick (orange) solid line) and PICO-2L[15] (thick (red) dashes). (b) The same for $\delta=23$ keV. In both plots $c^n/c^p=-0.03$ and $\rho_{DM}=0.3$ GeV/cm³.

the corresponding 90% C.L. upper bounds on σ_{ref} from other experiments. As in all the other plots here $c^n/c^p=-0.03$. Indeed, in the elastic case ($\delta=0$) of Fig.7(a) the constraints from bubble chambers and droplet detectors, all containing fluorine, are in strong tension to an interpretation of the DAMA modulation effect in terms of a WIMP signal. However, as shown in Fig.7(b) for $\delta=23$ keV, when m_{DM} and δ fall inside the solid (black) contour of Fig.4 all fluorine upper bounds are kinematically relaxed.

We conclude this Section by noting that, when $f(\vec{v})$ is identified with a Maxwellian distribution, in Figures 5 and 6(a) the $\tilde{\eta}_1^{est}(v_{min})$ modulated halo function traces very closely $\tilde{\eta}^{est}(v_{min})$ if v_{min} is in the range of the DAMA effect, i.e. the modulation amplitude fraction predicted in DAMA is very close to unity. This is at variance with the qualitative expectation that the modulated fraction is of order $\Delta v_{Earth}/v_{Earth} \simeq 0.07$. For P_1 the effect is quite dramatic although, as discussed in detail in Section 2, the two parameters m_{DM} and δ must be considerably tuned to verify the condition of Eq.(1.5) and are sensitive to the choice of v_{esc} . However, a large modulation fraction is also present inside the wider $\mathcal{D}_{Maxwellian} < 1$ contour: indeed, as shown in Fig. 6(a), the benchmark point P_2 , which is on the boundary of such region of the parameter space, has modulation fractions of order 50% in the DAMA v_{min} range. For this effect to happen it is clearly necessary that a combination of small m_{DM} and large δ drive v_{min} in DAMA to the large-velocity tail of $f(\vec{v})$. On the other hand, when the IDM parameter space is enlarged to the wider (red) dotted contour of Fig. 4 v_{min} moves to lower values where such large modulation fractions may not be necessarily expected. Indeed in Fig. 6(b) for the Maxwellian case (which is anyway excluded by the combined constraints from PICASSO, PICO-60 and PICO-2L) $\tilde{\eta}_1^{est}(v_{min}) \ll \tilde{\eta}^{est}(v_{min})$. On

the other hand when the the halo-independent analysis is applied $\tilde{\eta}^{est}(v_{min}) \simeq \tilde{\eta}_1^{est}(v_{min})$ is going to be eventually required at the boundary of the (red) dotted contour of Fig. 4 to evade the constraints on DAMA from other experiments, although deep in the allowed region smaller modulation amplitudes are allowed: for example, in Fig. 6(b) the halo-independent $\tilde{\eta}_1^{est}(v_{min})$ from DAMA is about 33% of the corresponding maximal $\tilde{\eta}^{est}(v_{min})$ allowed by the most stringent constraint (COUPP) represented by the lowest (crimson) long-dashed line.

When present, the details of the large-modulation effect in our scenario are expected to depend on the specific choice of the velocity distribution. In particular, the large-speed regime of $f(\vec{v})$ may correspond to sparsely populated regions in the WIMP phase space less likely to be well predicted by the gross approximation of a Maxwellian with a velocity cut-off: indeed, they may contain non-thermalized components difficult to predict in numerical simulations and dependent on the merger history of our Galaxy [41]. Nevertheless a large-velocity cut-off in $f(\vec{v})$ and a steep dependence of the halo function in the large v_{min} regime are features expected on quite general grounds, so that large modulated fractions should be considered a natural prediction of our scenario. In the following Section we will use a simple Maxwellian distribution cut-off at v_{esc} to capture at least qualitatively such features in order to address the issue of whether, if possible, such modulated fractions may be constrained or even already excluded in the DAMA data.

We close this Section observing that modulation fractions much larger than usually expected might be an attractive possibility when explaining DAMA. In fact a theoretical prediction of the modulation fraction $\Delta R_{[E'_1, E'_2]}/R_{[E'_1, E'_2]}$ allows to use the DAMA measurement of $\Delta R_{[E'_1, E'_2]}$ to get an estimation of the $R_{[E'_1, E'_2]}$ contribution of the signal to the time-averaged event spectrum measured by DAMA, and so, by difference, of the background contribution from radioactive contamination, neutrons and cosmic rays. The fact that the low-energy time-averaged count rate measured by DAMA is approximately flat, while instead the predicted $R_{[E'_1, E'_2]}$ usually depends exponentially on the recoil energy, has been used by some authors to claim that in some cases the resulting estimation of the background shows an energy dependence difficult to reconcile to what is expected by simulations [42]. Probably the many uncertainties of the latter do not allow to draw robust constraints anyway: however, large modulation fractions imply much smaller predictions for $R_{[E'_1, E'_2]}$ easing this potential tension.

5 Large modulation fractions: the Maxwellian case

In the previous Sections we pointed out that a natural prediction of our scenario is that the annual time-variation of the rate of WIMP-Na scatterings in DAMA can be much larger than usually expected and even approaching 100% of the time-averaged rate. In particular, this is expected to happen on quite general grounds if the kinematic condition (1.5) is verified, and can be verified quantitatively in the case of a Maxwellian WIMP velocity distribution.

It has been claimed in the literature that in such case a significant distortion of the time dependence of the expected rate from a cosine should be present[32]. In this Section we wish to elaborate more on this aspect. In order to be quantitative, we will explicitly adopt for $f(\vec{v})$ a Maxwellian distribution defined in the reference frame of the Galaxy with a cut for $|\vec{v}| < v_{esc}$, with the reference values $v_{rms} \simeq 270$ km/sec, $v_{esc}=550$ km/sec. Moreover, for definiteness in this Section we will adopt the set of IDM parameters $m_{DM}=11.4$ GeV and $\delta=23.7$ keV, which corresponds to the benchmark point P_1 in Fig.4 and maximizes the effect.

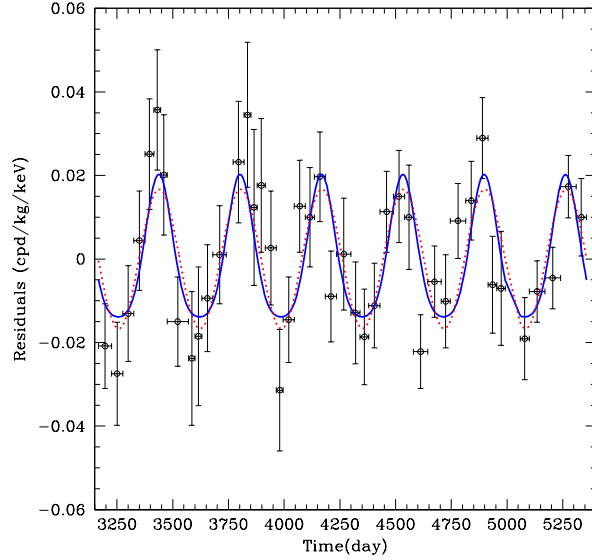


Figure 8. The data points represent the count-rate residuals measured by DAMA in the energy interval 2–4 keVee using an exposure of 0.87 ton \times year (from Fig. 1 of [1]). Solid (blue) line: theoretical prediction of the count-rate residuals for the benchmark point $P_1=(m_{DM}=11.4$ GeV, $\delta=23.7$ keV) assuming a Maxwellian velocity distribution when the product $\rho_{DM}\sigma_{ref}$ is set to the value which minimizes a χ -square with the 43 experimental data points; dotted (red) line: the same quantity for a cosine time dependence. For both theoretical predictions we have assumed a phase of the modulation corresponding to $t_0=152.5$ days (June 2nd).

In Figs.8 and 9 we show the annual modulation effect in time and frequency space comparing the predictions for benchmark P_1 to the DAMA data [1]. In particular, in Fig. 8 the data points are taken from Fig. 1 of [1] and represent the count-rate residuals measured by DAMA in the energy interval 2–4 keVee using an exposure of 0.87 ton \times year (corresponding to a total period of 2191 days and encompassing 6 complete annual modulation cycles). Since the full DAMA data are not available to analyze, we will use these data points for a comparison with our large-modulation scenario. In each data point the horizontal error bar represents the time intervals over which the detected count rate has been averaged (the data are averaged over 43 time intervals whose amplitude ranges from $\simeq 30$ to $\simeq 70$ days and which are shorter close to maxima and minima). The residuals are obtained by averaging the measured count rate in each time interval (after cuts to reduce the background) and subtracting the total average, which is obtained by dividing the total event sum over the complete period of data taking by the number of live days. In the same Figure the solid (blue) line represents the P_1 theoretical prediction calculated in the same way. This line has been calculated by fixing the product $\rho_{DM}\sigma_{ref}$ to the value which minimizes a χ -square with the 43 experimental data points. In the same figure the dotted (red) line represents the same quantity obtained by assuming for the residual a cosine time dependence. In both cases we have assumed a phase of the modulation corresponding to $t_0=152.5$ days (June 2nd). Indeed, in the P_1 prediction a distortion is clearly visible. However, the minimal χ -square in the two cases is 40.8 and 42.3 respectively, with 43-1 degrees of freedom: within the experimental errors the two time dependencies are undistinguishable.

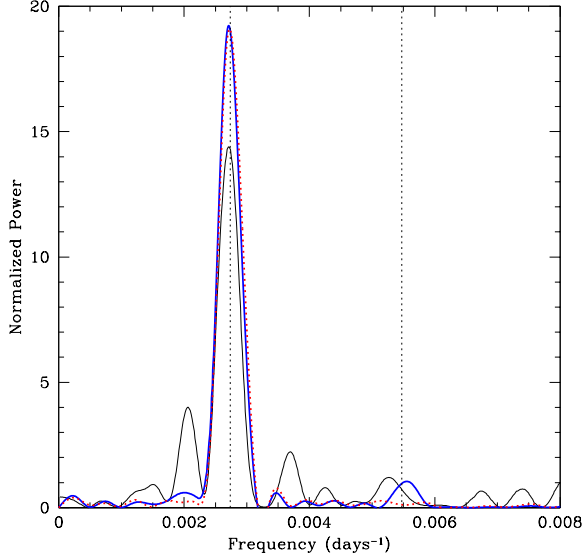


Figure 9. Thin (black) solid line: experimental DAMA determination of the normalized power spectrum in the energy interval $2 \text{ keV} \leq E_{ee} \leq 6 \text{ keV}$ and using an exposure of $0.87 \text{ ton} \times \text{year}$ (from Fig.2 of [1]); thick solid (blue) line: prediction of the same quantity for the P_1 benchmark; thick (red) dotted line: the same for a cosine time dependence.

The distortion visible in the time dependence of the model P_1 expected rate can be traced back to the fact that the latter can be written as a power expansion in terms of the small parameter $\Delta v_{Earth}/v_{Sun} \cos[2\pi t/T - t_0] \simeq 0.07 \cos[2\pi t/T - t_0]$:

$$\begin{aligned}
 S[t] &= S_0 + S_1 \frac{\Delta v_{Earth}}{v_{Sun}} \cos \left[\frac{2\pi}{T} t - t_0 \right] + S_2 \left(\frac{\Delta v_{Earth}}{v_{Sun}} \cos \left[\frac{2\pi}{T} t - t_0 \right] \right)^2 + \dots \\
 &= S_0 + \tilde{S}_1 \cos \left[\frac{2\pi}{T} t - t_0 \right] + \tilde{S}_2 \left(\cos \left[\frac{2\pi}{T} t - t_0 \right] \right)^2 + \dots
 \end{aligned} \tag{5.1}$$

In the case of large modulation fractions one has $S_0 \simeq \tilde{S}_1$ and when $\cos[2\pi/Tt - t_0] \simeq -1$, the cancellation between the first two terms in the power expansion implies dominance of \tilde{S}_2 , explaining the distortion in Fig.8. Nevertheless, due to the small ratio $\Delta v_{Earth}/v_{Sun}$ the term \tilde{S}_2 is always much smaller than S_0 and \tilde{S}_1 . In particular this implies that also in frequency space the contribution of the second harmonics remains necessarily small. This can be seen in Fig. 9, where the thin (black) solid line represents the experimental DAMA determination of the normalized power spectrum in the energy interval $2 \text{ keV} \leq E' \leq 6 \text{ keV}$ (taken from Fig.2 of [1]), while the thick solid (blue) line and the thick (red) dotted line show the predictions for the same quantity using the expected rate for P_1 (calculated with the same procedure of Fig.8) and a cosine time dependence, respectively: inspection of this figure confirms that the DAMA data are in substantial agreement with both the cosine dependence and the distorted one. So we conclude that, since the distortions in the time dependence of the annual modulation that arise in a natural way in our scenario are compatible to the DAMA data even for the extreme $\simeq 100\%$ case of benchmark P_1 , this is

also true in the remaining part of the parameter space, where this effect is expected to be milder.

We close this Section with a discussion of the energy dependence of the modulation amplitudes in our scenario. In Fig.10 the data points represent the determination of such quantities by DAMA. The procedure adopted to extract them from the experimental count rates is described in Ref.[1]: it consists in parameterizing the expected rate in terms of the sum of a constant part and a cosine-modulated one, i.e. $S(E', t) = B(E') + S_0(E') + S_m(E') \cos(2\pi t/T - t_0)$ (where $B(E')$ represents a time-independent unknown background) and minimizing a likelihood function with the data in terms of $B(E')$, $S_0(E')$ and $S_m(E')$, binning the data in $\Delta E' = q\Delta E_R = 0.5$ keVee intervals starting from 2 keVee (as can be seen from Fig.10 the bulk of the modulation excess is concentrated for $E' < 4$ keVee). The experimental determinations S_m^{exp} obtained in this way for the modulation amplitudes as a function of the recoil energy are then compared to the theoretical predictions S_m^{th} for a specific DM model.

However, when the time dependence of the count rate of a given DM candidate departs from a cosine the S_m^{th} definition deserves some care. In Fig. 10 we show different definitions of S_m^{th} for benchmark P_1 : the (red) long dashes represent the theoretical prediction of the difference $S_m^{diff}(E') = [S(E', t_{max}) - S(E', t_{min})]/2$, while the (blue) solid line represents the quantity $S_m^X(E')$ that, together with $S_0^X(E')$, minimizes the function $\chi^2[S_0^X(E'), S_m^X(E')] = \sum_t [S(E', t) - S_0^X(E') - S_m^X(E') \cos(2\pi t/T - t_0)]^2$ where $S(E', t)$ is the full calculation of the expected rate for P_1 as a function of time (notice that in this way $S_m^X/S_0^X > 1$ is possible, because the time-dependence of the rate is parameterized in terms of a "wrong" functional form: indeed, in the particular example of Figure 10 this ratio is slightly higher than unity in all the energy range⁹). Moreover, in the same Figure the (green) dotted line represents the quantity $S_m^\delta(E') \equiv \partial S(E', t)/\partial \eta \times \Delta \eta$ with $\eta = v_{Earth}/v_{Sun}$ and $\Delta \eta = \Delta v_{Earth}/v_{Sun}$. In case of a cosine time dependence of $S(E', t)$ the three definitions for the modulation amplitudes S_m^{diff} , S_m^X and S_m^δ coincide, but when the time dependence departs from a simple cosine the S_m^{th} 's whose definition is closer to the experimental S_m^{exp} amplitudes published by DAMA should be identified with the S_m^X 's (lacking a full minimization of the likelihood function of the data). Nevertheless, as can be seen in Fig. 10, the three determinations are very close to each other and their difference much smaller than the experimental errors. This justifies the use of the definition $S_m^{th} = S_m^{diff}$ for the theoretical predictions S_m^{th} of the modulated amplitudes that was implied by Eq.(3.3) and used in Section 4.

We conclude this Section by noting that, as anticipated, in Fig.10 the function $S_m^{th}[E']$ shows a maximum when $2 \text{ keVee} \lesssim E' \lesssim 3 \text{ keVee}$, which is in rough agreement to the experimental determinations $S_m^{exp}[E']$. As shown in Fig.11, where the Maxwellian η_1 (corresponding to the modulated halo function $\tilde{\eta}_1$ (3.3) with $\rho_{DM}\sigma_{ref}/m_{DM} \rightarrow 1$) is plotted as a function of the non-dimensional combination $x_{min} \equiv \sqrt{3/2}v_{min}/v_{rms}$, for elastic scattering this may be interpreted as a possible indication that the WIMP mass is particularly light ($m_{DM} \lesssim 10$ GeV), since this corresponds to the low x_{min} regime where the modulation amplitude shows a phase inversion just below the DAMA energy threshold[24]¹⁰. Interestingly, in the case of our inelastic scattering scenario the expected modulation amplitude $S_m^{th}[E']$ shows a maxi-

⁹If the function χ^2 is minimized imposing the condition $S_m^X/S_0^X \leq 1$ the modulated fraction of the signal turns out to be exactly 100%.

¹⁰The presence of a peak in the measured modulation amplitudes is the reason why the DAMA data, while showing for elastic scattering two local mass minima of the Likelihood, have a preference for the low-mass solution.

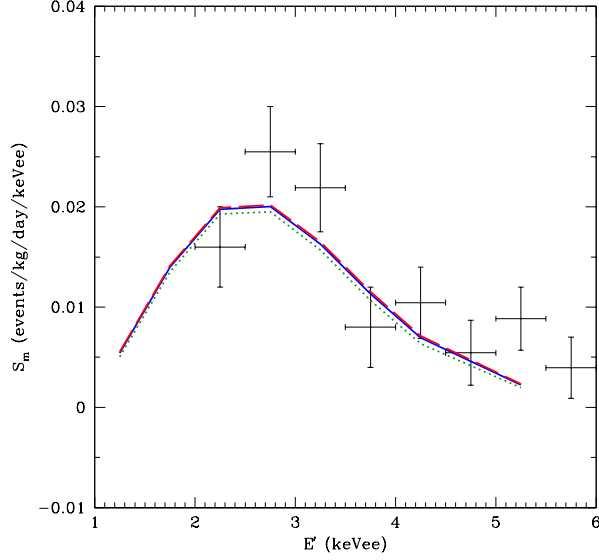


Figure 10. The data points show the DAMA modulation amplitudes as a function of the detected recoil energy E' (from Fig. 6 of Ref.[1]). The other curves show theoretical predictions of the modulation amplitudes S_m^{th} for the benchmark point P_1 using different definitions (see text): (red) long dashes: $S_m^{th}=S_m^{diff}(E') \equiv [S(E', t_{max}) - S(E', t_{min})]/2$; (blue) solid line: $S_m^{th}=S_m^x(E')$ minimizing the function $\chi^2 = \sum_t [S(E', t) - S_0^x(E') - S_m^x(E') \cos(2\pi t/T - t_0)]^2$ with $S(E', t)$ the full calculation of the expected rate; (green) dotted line: $S_m^{th}=S_m^\delta(E') \equiv \partial S(E', t)/\partial \eta \times \Delta \eta$ with $\eta = v_{Earth}/v_{Sun}$ and $\Delta \eta = \Delta v_{Earth}/v_{Sun}$.

imum within the DAMA energy range for a completely different reason. In fact in this case large x_{min} values are involved, in particular beyond the maximum of η_1 , in a regime where the latter is decreasing with v_{min} and so is maximized when $v_{min}=v_{min}^{*Na}$ (corresponding for the benchmark point P_1 to $x_{min}^{*Na} \simeq 3.44$ as shown in Fig.11). As a consequence of this $\tilde{\eta}_1$ shows a maximum when $E'=E_{ee}^{*Na}=qE_R^{*Na}$ with E_R^* defined in Eq.(1.4), i.e. the maximum in the modulation amplitude detected by DAMA corresponds to WIMPs whose minimal incoming speed matches the kinematic threshold of inelastic upscatters. In particular, for the benchmark point P_1 one has $E_{ee}^* \simeq 2.5$, keVee and the fact that this value falls right in the energy interval where the DAMA signal is detected is not a coincidence, but descends from the requirement of Eq.(1.5). In this case, however, the modulation amplitude at very low energies vanishes instead of turning negative, because below E_{ee}^{*Na} the halo function $\tilde{\eta}_1(v_{min})$ is mapped in the same v_{min} intervals than above E_{ee}^{*Na} , where $\tilde{\eta}_1(v_{min}) \geq 0$: this may allow for a possible discrimination among the two scenarios in a future low-threshold analysis of the DAMA data [25]¹¹.

6 Conclusions

In the present paper we have discussed a scenario where the DAMA modulation effect is explained by a WIMP which upscatters inelastically to a heavier state and predominantly

¹¹The change of the modulation amplitude can also be affected by the gravitational focusing of the Sun[43–45].

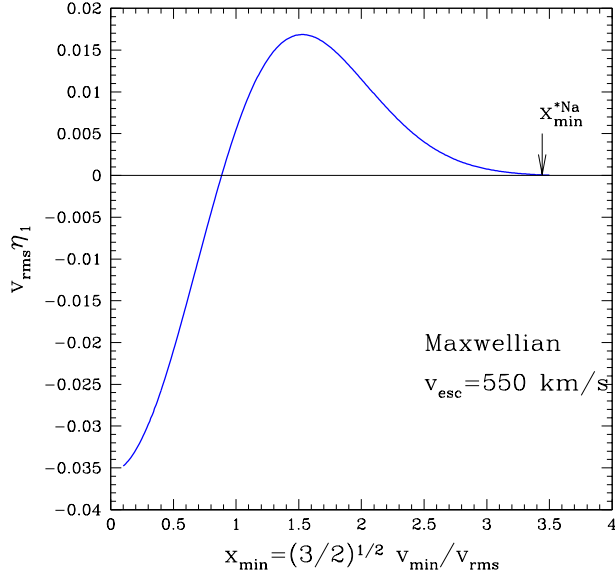


Figure 11. Modulated halo function η_1 (corresponding to the $\tilde{\eta}_1$ of Eq.(3.3) with $\rho_{DM}\sigma_{ref}/m_{DM}\rightarrow 1$) as a function of the non-dimensional ratio $x_{min} \equiv \sqrt{3/2}v_{min}/v_{rms}$ for a Maxwellian distribution with $v_{rms}=270$ km/sec and $v_{esc}=550$ km/sec. The arrow shows the position of $x_{min}^{*Na}=\sqrt{3/2}v_{min}^{*Na}/v_{rms}$ for the benchmark point P_1 , i.e. for $m_{DM}=11.4$ GeV and $\delta=23.7$ keV.

couples to the spin of protons. In this scenario constraints from xenon and germanium targets are evaded dynamically, due to the suppression of the WIMP coupling c^n to neutrons compared to the corresponding one c^p to protons and we have shown that, in order to evade the constraint from LUX, the ratio c^n/c^p must be tuned to a small but non-vanishing value, which depends on which nuclear form factor is adopted. On the other hand, the limits from fluorine targets are evaded by a kinematical mechanism, because a combination of small values of the WIMP mass m_{DM} and large values of the mass splitting δ between the light and the heavy WIMP states drives the minimal WIMP incoming speed v_{min}^{*F} required to trigger upscatters off fluorine either beyond the cut-off velocity v_{cut}^{lab} of the WIMP distribution $f(\vec{v}_T)$ in the lab frame or very close to it. On the other hand, WIMP scatterings off sodium can still explain the yearly modulation effect in DAMA because the corresponding v_{min}^{*Na} is always smaller, since the sodium atomic mass is larger than that of fluorine. In summary: $v_{min}^{*Na} < v_{cut}^{lab} < v_{min}^{*F}$. The corresponding requirements for m_{DM} and δ can be combined consistently to those requiring that scatterings off iodine in COUPP are suppressed by a similar kinematic mechanism ($v_{min}(E^{COUPP}) > v_{cut}^{lab}$), since the latter experiment can potentially constrain our scenario, being sensitive to WIMP-proton scatterings and having a low recoil energy threshold.

We have analyzed quantitatively the available data from direct detection experiments either by fixing $f(\vec{v})$ to a Maxwellian distribution and factorizing a reference WIMP-nucleon point-like cross section σ_{ref} , or adopting instead a halo-independent approach, where the dependence of the expected signal on the specific choice of $f(\vec{v})$ is factorized in a halo function $\tilde{\eta}$ and its corresponding modulated one $\tilde{\eta}_1$, with the requirement $\tilde{\eta}_1 \leq \tilde{\eta}$. In the Maxwellian analysis we have made the usual identification of v_{cut}^{lab} with the Galactic escape velocity boosted in the Earth's rest frame, while in the halo-independent one we have instead made

the conservative assumption that v_{cut}^{lab} is the maximal v_{min} value corresponding to the recoil energy range of the DAMA modulation effect. The latter procedure corresponds to adopting the minimal halo function explaining DAMA and compatible to the requirement of being a decreasing function of v_{min} , and leads to laxer constraints in the m_{DM} - δ plane when used to calculate expected signals in null experiments.

The systematic scan of the m_{DM} - δ parameter space using a quantitative compatibility factor $\mathcal{D}_{Maxwellian}$ for the Maxwellian case and \mathcal{D} for the halo-independent one (both containing a full treatment of the expected rates in all experiments) has shown that in both cases the kinematic requirements $v_{min}^{*Na} < v_{cut}^{lab} < v_{min}^{*F}$, $v_{min}(E^{COUPP}) > v_{cut}^{lab}$ are sufficient to find allowed configurations but not strictly necessary, since the allowed regions are significantly larger than the kinematic ones, especially for the halo-independent case. Our results are summarized in Fig.4, which shows that for the Maxwellian case allowed configurations encompass the ranges $10 \text{ GeV} \lesssim m_{DM} \lesssim 13.5 \text{ GeV}$, $19.8 \text{ keV} \lesssim \delta \lesssim 26.5 \text{ keV}$, while in the case of a halo-independent analysis such region enlarges considerably to $9.6 \text{ GeV} \lesssim m_{DM} \lesssim 31.3 \text{ GeV}$, $8.4 \text{ keV} \lesssim \delta \lesssim 27.3 \text{ keV}$ ¹².

We have shown that in our scenario the same kinematic mechanism that suppresses the response to WIMP scatterings off fluorine compared to sodium can lead in a natural way to a yearly modulation of the signal in DAMA much larger than usually expected and which can approach 100% of the time-averaged part. This is always true for the allowed configurations in the Maxwellian case, while configurations allowed by the halo-independent treatment exist for which this effect may not be present. However, at the boundary of the parameter region allowed by the halo-independent analysis large modulation fractions are required to evade the constraints on DAMA from other experiments.

Assuming a Maxwellian distribution we have shown that the large modulated fractions of the signal arising in our scenario imply a departure from the usual cosine time dependence, but even in the most extreme cases the DAMA data is not sensitive to this distortion, both in time and frequency space. On the other hand, when the modulated fraction is large the signal contribution to the time-averaged DAMA measured count-rates can be much smaller than usually assumed, easing possible tension with DAMA background estimations existing in the literature.

In our scenario the DAMA modulation effect can be explained in terms of large values of v_{min} . In this regime the Maxwellian modulated halo function $\tilde{\eta}_1$ decreases with v_{min} and so is maximized by $v_{min} = v_{min}^{*Na}$. Moreover, the requirement $v_{min}^{*Na} < v_{cut}^{lab} < v_{min}^{*F}$ automatically implies that the recoil energy E_R^{*Na} which corresponds to v_{min}^{*Na} falls in the DAMA energy range. This provides a simple explanation of the maximum in the modulation amplitude detected by DAMA in terms of WIMPs whose v_{min} matches the kinematic threshold for inelastic upscatters. Interestingly, while for the elastic case the presence of a maximum suggests an inversion of the modulation phase below the present DAMA energy threshold, this does not happen for inelastic scattering. This may possibly allow for a discrimination between the two scenarios in a future low-threshold analysis of the DAMA data.

¹²In our analysis we have assumed that the DAMA signal is concentrated in the range $2 \text{ keVee} \leq E_{ee}^{DAMA} \leq 4 \text{ keVee}$. Requiring a positive signal also in the energy range $4 \text{ keVee} \leq E_{ee}^{DAMA} \leq 6 \text{ keVee}$ would lower the kinematic upper-left boundaries of the allowed regions of Fig.4 without affecting the remaining parts.

Acknowledgments

This work was supported by the National Research Foundation of Korea(NRF) grant funded by the Korea government(MOE) (No. 2011-0024836).

Note added in proof. After completing our analysis new improved WIMP direct detection experimental constraints were published by LUX [46] and PICO-2L [47]. As far as the new LUX result is concerned it does not affect our conclusions due to the Xe-phobic nature of our WIMP candidate for the choice of the c^n/c^p ratio adopted in our analysis. As far as the new PICO-2L result is concerned, while the allowed kinematic regions described in Section 2 are necessarily not affected, since in such kinematic ranges *any* fluorine target turns blind to WIMP particles, its systematic inclusion in the extended numerical analysis of Section 4 may somewhat affect the shape and extension of the boundaries of the regions shown in Fig.4.

A Experimental inputs

Compared to the analysis of Ref. [21], to which we refer for all relevant details, in the present analysis we include two additional experiments: the recent analyses by CDMS II [11] and PICO-60 [16].

As far as the analysis of CDMS II is concerned, we consider only the "classic" analysis with 10 keV threshold (see first entry of Table II of Ref.[11]), with the two WIMP candidates shown in Table I and the efficiency taken from the black solid line of the top panel of Fig. 10 of the same paper.

PICO-60 is a bubble-chamber filled with 36.8 kg of CF_3I . For each of its operating thresholds (7 keV, 8.2 keV, 9.6 keV, 11.5 keV, 13.0 keV, 14.5 keV, 17.0 keV) we have used the exposures obtained by combining the livetimes shown in Table 1 of Ref. [16] with the overall acceptance after cuts of 48.2%. No WIMP-event candidates survive after the cuts, with a background estimation of 1.0 neutron-induced single bubble events and a 90% C.L. upper bound of 2.33 events [48].

References

- [1] **DAMA, LIBRA** Collaboration, R. Bernabei et al., *New results from DAMA/LIBRA*, *Eur. Phys. J.* **C67** (2010) 39–49, [[arXiv:1002.1028](#)].
- [2] **LUX** Collaboration, D. S. Akerib et al., *First results from the LUX dark matter experiment at the Sanford Underground Research Facility*, *Phys. Rev. Lett.* **112** (2014) 091303, [[arXiv:1310.8214](#)].
- [3] **XENON100** Collaboration, E. Aprile et al., *Dark Matter Results from 225 Live Days of XENON100 Data*, *Phys. Rev. Lett.* **109** (2012) 181301, [[arXiv:1207.5988](#)].
- [4] **XENON10** Collaboration, J. Angle et al., *A search for light dark matter in XENON10 data*, *Phys. Rev. Lett.* **107** (2011) 051301, [[arXiv:1104.3088](#)]. [Erratum: *Phys. Rev. Lett.*110,249901(2013)].
- [5] S. C. Kim et al., *New Limits on Interactions between Weakly Interacting Massive Particles and Nucleons Obtained with CsI(Tl) Crystal Detectors*, *Phys. Rev. Lett.* **108** (2012) 181301, [[arXiv:1204.2646](#)].
- [6] Y. Kim, *Recent progress in KIMS experiment, talk given at 13th International Conference on Topics in Astroparticle and Underground Physics, September 8–13 2013, Asilomar, California USA (TAUP2013)*, .

- [7] H. S. Lee et al., *Search for Low-Mass Dark Matter with CsI(Tl) Crystal Detectors*, *Phys. Rev. D* **90** (2014), no. 5 052006, [[arXiv:1404.3443](#)].
- [8] **CDMS-II** Collaboration, Z. Ahmed et al., *Results from a Low-Energy Analysis of the CDMS II Germanium Data*, *Phys. Rev. Lett.* **106** (2011) 131302, [[arXiv:1011.2482](#)].
- [9] **SuperCDMS** Collaboration, R. Agnese et al., *Search for Low-Mass Weakly Interacting Massive Particles Using Voltage-Assisted Calorimetric Ionization Detection in the SuperCDMS Experiment*, *Phys. Rev. Lett.* **112** (2014), no. 4 041302, [[arXiv:1309.3259](#)].
- [10] **SuperCDMS** Collaboration, R. Agnese et al., *Search for Low-Mass Weakly Interacting Massive Particles with SuperCDMS*, *Phys. Rev. Lett.* **112** (2014), no. 24 241302, [[arXiv:1402.7137](#)].
- [11] **SuperCDMS** Collaboration, R. Agnese et al., *Improved WIMP-search reach of the CDMS II germanium data*, *Phys. Rev. D* **92** (2015), no. 7 072003, [[arXiv:1504.05871](#)].
- [12] M. Felizardo et al., *Final Analysis and Results of the Phase II SIMPLE Dark Matter Search*, *Phys. Rev. Lett.* **108** (2012) 201302, [[arXiv:1106.3014](#)].
- [13] **COUPP** Collaboration, E. Behnke et al., *First Dark Matter Search Results from a 4-kg CF₃I Bubble Chamber Operated in a Deep Underground Site*, *Phys. Rev. D* **86** (2012), no. 5 052001, [[arXiv:1204.3094](#)]. [Erratum: *Phys. Rev. D* **90**, no. 7, 079902 (2014)].
- [14] **PICASSO** Collaboration, S. Archambault et al., *Constraints on Low-Mass WIMP Interactions on ¹⁹F from PICASSO*, *Phys. Lett. B* **711** (2012) 153–161, [[arXiv:1202.1240](#)].
- [15] **PICO** Collaboration, C. Amole et al., *Dark Matter Search Results from the PICO-2L C₃F₈ Bubble Chamber*, *Phys. Rev. Lett.* **114** (2015), no. 23 231302, [[arXiv:1503.00008](#)].
- [16] **PICO** Collaboration, C. Amole et al., *Dark Matter Search Results from the PICO-60 CF₃I Bubble Chamber*, *Submitted to: Phys. Rev. D* (2015) [[arXiv:1510.07754](#)].
- [17] P. Ullio, M. Kamionkowski, and P. Vogel, *Spin dependent WIMPs in DAMA?*, *JHEP* **07** (2001) 044, [[hep-ph/0010036](#)].
- [18] E. Del Nobile, G. B. Gelmini, A. Georgescu, and J.-H. Huh, *Reevaluation of spin-dependent WIMP-proton interactions as an explanation of the DAMA data*, *JCAP* **1508** (2015), no. 08 046, [[arXiv:1502.07682](#)].
- [19] M. Freytsis and Z. Ligeti, *On dark matter models with uniquely spin-dependent detection possibilities*, *Phys. Rev. D* **83** (2011) 115009, [[arXiv:1012.5317](#)].
- [20] C. Arina, E. Del Nobile, and P. Panci, *Dark Matter with Pseudoscalar-Mediated Interactions Explains the DAMA Signal and the Galactic Center Excess*, *Phys. Rev. Lett.* **114** (2015) 011301, [[arXiv:1406.5542](#)].
- [21] S. Scopel, K.-H. Yoon, and J.-H. Yoon, *Generalized spin-dependent WIMP-nucleus interactions and the DAMA modulation effect*, *JCAP* **1507** (2015), no. 07 041, [[arXiv:1505.01926](#)].
- [22] D. Tucker-Smith and N. Weiner, *Inelastic dark matter*, *Phys. Rev. D* **64** (2001) 043502, [[hep-ph/0101138](#)].
- [23] We adopt here the conventional value $v_{loc}=220$ km/s which is used in most Dark Matter direct detection experimental papers. For a more recent determination of v_{loc} see, for instance, Ref. [[34](#)].
- [24] M. J. Lewis and K. Freese, *The Phase of the annual modulation: Constraining the WIMP mass*, *Phys. Rev. D* **70** (2004) 043501, [[astro-ph/0307190](#)].
- [25] R. Bernabei et al., *New Results from DAMA/LIBRA: Final Model-Independent Results of Dama/Libra-Phase1 and Perspectives of Phase2*, *Frascati Phys. Ser.* **58** (2014) 41.
- [26] P. J. Fox, J. Liu, and N. Weiner, *Integrating Out Astrophysical Uncertainties*, *Phys. Rev. D* **83** (2011) 103514, [[arXiv:1011.1915](#)].

- [27] C. McCabe, *DAMA and CoGeNT without astrophysical uncertainties*, *Phys. Rev.* **D84** (2011) 043525, [[arXiv:1107.0741](#)].
- [28] P. Gondolo and G. B. Gelmini, *Halo independent comparison of direct dark matter detection data*, *JCAP* **1212** (2012) 015, [[arXiv:1202.6359](#)].
- [29] E. Del Nobile, G. B. Gelmini, P. Gondolo, and J.-H. Huh, *Halo-independent analysis of direct detection data for light WIMPs*, *JCAP* **1310** (2013) 026, [[arXiv:1304.6183](#)].
- [30] E. Del Nobile, G. B. Gelmini, P. Gondolo, and J.-H. Huh, *Update on Light WIMP Limits: LUX, lite and Light*, *JCAP* **1403** (2014) 014, [[arXiv:1311.4247](#)].
- [31] S. Scopel and K. Yoon, *A systematic halo-independent analysis of direct detection data within the framework of Inelastic Dark Matter*, *JCAP* **1408** (2014) 060, [[arXiv:1405.0364](#)].
- [32] K. Freese, M. Lisanti, and C. Savage, *Colloquium: Annual modulation of dark matter*, *Rev. Mod. Phys.* **85** (2013) 1561–1581, [[arXiv:1209.3339](#)].
- [33] M. C. Smith et al., *The RAVE Survey: Constraining the Local Galactic Escape Speed*, *Mon. Not. Roy. Astron. Soc.* **379** (2007) 755–772, [[astro-ph/0611671](#)].
- [34] F. Nesti and P. Salucci, *The Dark Matter halo of the Milky Way*, *AD 2013*, *JCAP* **1307** (2013) 016, [[arXiv:1304.5127](#)].
- [35] S. Chaudhury, P. Bhattacharjee, and R. Cowsik, *Direct detection of WIMPs : Implications of a self-consistent truncated isothermal model of the Milky Way’s dark matter halo*, *JCAP* **1009** (2010) 020, [[arXiv:1006.5588](#)].
- [36] A. L. Fitzpatrick, W. Haxton, E. Katz, N. Lubbers, and Y. Xu, *The Effective Field Theory of Dark Matter Direct Detection*, *JCAP* **1302** (2013) 004, [[arXiv:1203.3542](#)].
- [37] N. Anand, A. L. Fitzpatrick, and W. C. Haxton, *Weakly interacting massive particle-nucleus elastic scattering response*, *Phys. Rev.* **C89** (2014), no. 6 065501, [[arXiv:1308.6288](#)].
- [38] S. Scopel and J.-H. Yoon, *Effective scalar four-fermion interaction for Ge-phobic exothermic dark matter and the CDMS-II Silicon excess*, *Phys. Rev.* **D91** (2015), no. 1 015019, [[arXiv:1411.3683](#)].
- [39] N. Bozorgnia, J. Herrero-Garcia, T. Schwetz, and J. Zupan, *Halo-independent methods for inelastic dark matter scattering*, *JCAP* **1307** (2013) 049, [[arXiv:1305.3575](#)].
- [40] M. T. Ressell and D. J. Dean, *Spin dependent neutralino - nucleus scattering for A approximately 127 nuclei*, *Phys. Rev.* **C56** (1997) 535–546, [[hep-ph/9702290](#)].
- [41] M. Vogelsberger, A. Helmi, V. Springel, S. D. M. White, J. Wang, C. S. Frenk, A. Jenkins, A. D. Ludlow, and J. F. Navarro, *Phase-space structure in the local dark matter distribution and its signature in direct detection experiments*, *Mon. Not. Roy. Astron. Soc.* **395** (2009) 797–811, [[arXiv:0812.0362](#)].
- [42] V. A. Kudryavtsev, M. Robinson, and N. J. C. Spooner, *The expected background spectrum in NaI dark matter detectors and the DAMA result*, *Astropart. Phys.* **33** (2010) 91–96, [[arXiv:0912.2983](#)].
- [43] S. K. Lee, M. Lisanti, A. H. G. Peter, and B. R. Safdi, *Effect of Gravitational Focusing on Annual Modulation in Dark-Matter Direct-Detection Experiments*, *Phys. Rev. Lett.* **112** (2014), no. 1 011301, [[arXiv:1308.1953](#)].
- [44] N. Bozorgnia and T. Schwetz, *Is the effect of the Sun’s gravitational potential on dark matter particles observable?*, *JCAP* **1408** (2014) 013, [[arXiv:1405.2340](#)].
- [45] E. Del Nobile, G. B. Gelmini, and S. J. Witte, *Gravitational Focusing and Substructure Effects on the Rate Modulation in Direct Dark Matter Searches*, *JCAP* **1508** (2015), no. 08 041, [[arXiv:1505.07538](#)].

- [46] **LUX** Collaboration, D. S. Akerib et al., *Improved WIMP scattering limits from the LUX experiment*, [arXiv:1512.03506](#).
- [47] **PICO** Collaboration, C. Amole et al., *Improved Dark Matter Search Results from PICO-2L Run-2*, [arXiv:1601.03729](#).
- [48] G. J. Feldman and R. D. Cousins, *A Unified approach to the classical statistical analysis of small signals*, *Phys. Rev.* **D57** (1998) 3873–3889, [[physics/9711021](#)].